



RESEARCH ARTICLE

10.1029/2019MS001665

Key Points:

- A pilot reanalysis over the Tibetan Plateau using the PSU WRF-EnKF system was developed and evaluated against independent soundings and satellite observations as well as ERA-Interim and ERA5
- The pilot reanalysis had clear advantage in atmospheric humidity than existing global reanalysis
- The subsequent downscaled precipitation forecasts from the pilot reanalysis compared favorably against those from the global reanalyses of ERA-Interim and ERA5

Correspondence to:

X. Chen,
xzc55@psu.edu

Citation:

He, J., Zhang, F., Chen, X., Bao, X., Chen, D., Kim, H. M., et al. (2019). Development and evaluation of an ensemble-based data assimilation system for regional reanalysis over the Tibetan Plateau and surrounding regions. *Journal of Advances in Modeling Earth Systems*, 11, 2503–2522. <https://doi.org/10.1029/2019MS001665>











Received 18 FEB 2019

Accepted 8 JUL 2019

Accepted article online 16 JUL 2019

Published online 5 AUG 2019

Development and Evaluation of an Ensemble-Based Data Assimilation System for Regional Reanalysis Over the Tibetan Plateau and Surrounding Regions

Jie He^{1,2} , Fuqing Zhang^{2,3} , Xingchao Chen² , Xinghua Bao⁴ , Deliang Chen^{5,6} , Hyun Mee Kim⁷ , Hui-Wen Lai⁵, L. Ruby Leung⁸ , Xulin Ma¹, Zhiyong Meng⁹ , Tinghai Ou⁵ , Ziniu Xiao¹⁰, Eun-Gyeong Yang⁷, and Kun Yang¹¹ 

¹Collaborative Innovation Center on Forecast and Evaluation of Meteorological Disasters, Key Laboratory of Meteorological Disaster, Nanjing University of Information Science and Technology, Nanjing, China, ²Department of Meteorology and Atmospheric Science, and Center for Advanced Data Assimilation and Predictability Techniques, Pennsylvania State University, University Park, PA, USA, ³Deceased 19 July 2019, ⁴State Key Laboratory of Severe Weather, Chinese Academy of the Meteorological Sciences, Beijing, China, ⁵Department of Earth Sciences, University of Gothenburg Gothenburg, Sweden, ⁶CAS Center for Excellence in Tibetan Plateau Earth Sciences, Chinese Academy of Sciences, Beijing, China, ⁷Department of Atmospheric Sciences, Yonsei University, Seoul, South Korea, ⁸Pacific Northwest National Laboratory, Richland, WA, USA, ⁹Department of Atmospheric and Oceanic Sciences, School of Physics, Peking University, Beijing, China, ¹⁰State Key Laboratory of Numerical Modeling for Atmospheric Sciences and Geophysical Fluid Dynamics, Institute of Atmospheric Physics, Chinese Academy of Sciences, Beijing, China, ¹¹Ministry of Education Key Laboratory for Earth System Modeling, Department of Earth System Science, Tsinghua University, Beijing, China

Abstract The Tibetan Plateau is regarded as the Earth's Third Pole, which is the source region of several major rivers that impact more 20% the world population. This high-altitude region is reported to have been undergoing much greater rate of weather changes under global warming, but the existing reanalysis products are inadequate for depicting the state of the atmosphere, particularly with regard to the amount of precipitation and its diurnal cycle. An ensemble Kalman filter (EnKF) data assimilation system based on the limited-area Weather Research and Forecasting (WRF) model was evaluated for use in developing a regional reanalysis over the Tibetan Plateau and the surrounding regions. A 3-month prototype reanalysis over the summer months (June–August) of 2015 using WRF-EnKF at a 30-km grid spacing to assimilate nonradiance observations from the Global Telecommunications System was developed and evaluated against independent sounding and satellite observations in comparison to the ERA-Interim and fifth European Centre for Medium-Range Weather Forecasts Reanalysis (ERA5) global reanalysis. Results showed that both the posterior analysis and the subsequent 6- to 12-hr WRF forecasts of the prototype regional reanalysis compared favorably with independent sounding observations, satellite-based precipitation versus those from ERA-Interim and ERA5 during the same period. In particular, the prototype regional reanalysis had clear advantages over the global reanalyses of ERA-Interim and ERA5 in the analysis accuracy of atmospheric humidity, as well as in the subsequent downscale-simulated precipitation intensity, spatial distribution, diurnal evolution, and extreme occurrence.

1. Introduction

The Tibetan Plateau (TP), the highest mountain with the most complex topography, is known as the Third Pole of the world (Yao et al., 2019). A recent assessment of environmental changes over the TP shows that the regional warming rate over the last 50 years has been much larger than the global mean and those at similar latitudes, which caused a wide range of environmental changes such as ecosystem and water cycle (Chen et al., 2015). The TP encapsulates the most widespread effects on the regional and global water cycles (Xu et al., 2008; Yang et al., 2014) and is a key factor driving the Asian monsoon (Liu & Dong, 2013; Zhang et al., 2015). However, the physical mechanisms of atmospheric processes over the TP are still not well understood due to the complex terrain and harsh environment, which make observations of the atmosphere over the TP exceptionally difficult. Available satellite data indicate that spatial scale of variabilities in surface temperature and precipitation in the region can be extremely small (Chen et al., 2016). In addition, it is still a

©2019. The Authors.

This is an open access article under the terms of the Creative Commons Attribution-NonCommercial-NoDerivs License, which permits use and distribution in any medium, provided the original work is properly cited, the use is non-commercial and no modifications or adaptations are made.

huge challenge for numerical models to accurately simulate the atmospheric processes over complex topography, especially for mesoscale and regional systems.

Several major field campaigns (Ma et al., 2008; Zhang et al., 2012) aimed at deepening our understanding of atmospheric processes over the TP have been performed since 1979 (Tao et al., 1986). These include the ongoing Third Tibetan Plateau Atmospheric Scientific Experiment (TIPEX-III) that was initiated formally in 2013 (Zhao et al., 2018). However, observational data sets from field campaigns are limited by their sparse spatial and temporal coverage, in particular at the climatic timescales. Consequently, atmospheric reanalyses are often used instead of observations to explore the scientific conundrums over the TP. In addition, reanalysis has a wide range of application in atmospheric science such as monitoring climate conditions, detecting climate change, and providing data as inputs to climate models.

To provide a comprehensive characterization of the atmospheric states, global and regional reanalyses are generally generated by integrating all applicable observations into numerical weather prediction models through data assimilation methods. For instance, various generations of global reanalysis data sets including ERA-15 (Gibson et al., 1997), ERA-40 (Uppala et al., 2005), ERA-Interim (Berrisford et al., 2009; Dee et al., 2011), and the new fifth European Centre for Medium-Range Weather Forecasts Reanalysis (ERA5; Hersbach & Dee, 2016) have been released by the European Centre for Medium-Range Weather Forecasts. Meanwhile, the global atmosphere Reanalysis 1 (Kalnay et al., 1996; Kistler et al., 2001) spanning the period from 1948 to present was developed by the National Center for Environmental Prediction (NCEP) and National Center for Atmospheric Research using three-dimensional variational (3DVAR) data assimilation technology; this had subsequently been updated to Reanalysis 2 (Kanamitsu et al., 2002) with newer generation models and data assimilation techniques ingesting more observations. Also using the 3DVAR method, the Global Modeling and Assimilation Office of National Aeronautics and Space Administration has updated the Modern-Era Retrospective Analysis for Research and Applications (MERRA; Rienecker et al., 2011) to version 2 (MERRA-2; Gelaro et al., 2017). The Japanese 25-year Reanalysis (JRA-25; Onogi et al., 2007) with data from 1979 to 2004 and focusing on the Asian areas is produced by the Japan Meteorological Agency. JRA-25 has been extended to the more sophisticated Japanese 55-year Reanalysis in recent years (Ebita et al., 2011; Harada et al., 2016; Kobayashi et al., 2015).

Aside from the above global reanalysis projects, some high-resolution regional reanalysis projects were also launched to better resolve regional mesoscale processes, such as the North American Regional Reanalysis (Mesinger et al., 2006) of NCEP and Uncertainties in Ensembles of Regional Re-Analyses (Bach et al., 2016; Niermann et al., 2017). The East Asia Regional Reanalysis (Yang & Kim, 2017, 2019) was developed using a four-dimensional variational (4DVAR) data assimilation technique (Courtier et al., 1994; Rabier et al., 2000) by the Korea Meteorological Administration. Zhang et al. (2017) also produced a competitive regional reanalysis over mainland China by using the Gridpoint Statistical Interpolation data assimilation system and the Advanced Research WRF (ARW-WRF; Skamarock et al., 2008) model. Recently, the regional Indian Monsoon Data Assimilation and Analysis (Mahmood et al., 2014, 2018), with an emphasis of support in the study of the Asian monsoon characteristics over the Indian subcontinent, has been developed using the 4DVAR method by the Met Office, the National Centre for Medium Range Weather Forecasting, and the India Meteorological Department.

Although the regional reanalyses, including those not mentioned above, have played an important role in regional weather and climate studies, reliable high-resolution regional reanalysis over the TP is still lacking, which is at least in part due to the scarcity of observations over this region and the complexity of thermodynamic and dynamic effects induced by high terrains (Bao & Zhang, 2013; Wang & Zeng, 2012). Most regional reanalyses mentioned above do not even include the TP region. Meanwhile, model configurations and data assimilation techniques are key factors that can affect the quality and stability of reanalysis over the TP. Of later, the High Asia Reanalysis (Curio et al., 2015; Maussion et al., 2011) was produced by dynamical downscaling method using the WRF-ARW model driven by the NCEP Final (FNL) data from the GFS operational model. Even without data assimilation, increasing the spatial resolution using downscaling can improve the model's ability to resolve processes at the mesoscale that are important for precipitation over the TP. Nevertheless, since the performance of dynamical downscaling can be critically dependent on the quality of driving fields from global/regional reanalysis (Hu et al., 2018), it is necessary to explore the added benefits of alternative, TP-specific reanalysis using moderate-to-high resolution nonhydrostatic regional models, and advanced data assimilation approaches.

In this study, the Pennsylvania State University (PSU) WRF-EnKF system (Meng & Zhang, 2007; Meng & Zhang, 2008a, 2008b; Weng & Zhang, 2012; Zhang et al., 2006; Zhang et al., 2009; Zhang et al., 2011) was used to produce a regional atmospheric reanalysis at a 30-km grid spacing over the TP and surrounding areas. The time period of this pilot reanalysis system for the development and evaluation herein was the summer (June–August) of 2015, which will be extended to a longer time period in the future to produce a newer generation Tibetan Plateau Regional Reanalysis. Among studies of reanalysis systems, very few reanalysis projects with the exception of the Twentieth Century Reanalysis (Compo et al., 2011) generated by the Earth System Research Laboratory of National Oceanic and Atmospheric Administration (NOAA) used the EnKF method. Notably, in spite of the inclusion of 10 members on a coarser grid, the uncertainty estimate of ERA5 produced by the Ensemble of Data Assimilations system (Isaksen et al., 2010) is in essence generated using the 4DVAR method. Our goal for developing a regional, higher-resolution TP reanalysis by using EnKF method is to provide a more accurate estimate of atmospheric states over the TP, particularly for the regional-scale water cycle and precipitation that have profound consequences on the human society and ecosystems.

The design of the experiments and data used in the current study are presented in section 2, including a detailed description of the ensemble assimilation system, model configurations, and the observations used for data assimilation and verifications. Diagnostic methods for the WRF-EnKF reanalysis are described in section 3. Finally, evaluation of the WRF-EnKF reanalysis in comparison to ERA-Interim, ERA5 and the summary remarks are presented in sections 4 and 5, respectively.

2. Experimental Design

2.1. The WRF-EnKF Data Assimilation System

An intermediate-resolution regional reanalysis over the TP was developed using the PSU WRF-EnKF system that features coupling between the ARW-WRF (version 3.8.1) model and the EnKF data assimilation system. As a state-of-the-art data assimilation technique, the ensemble Kalman filter methodology has been widely used in atmospheric sciences in particular for numerical weather prediction (Houtekamer & Zhang, 2016). In light of its advantages, a 40-member ensemble was performed to produce the pilot reanalysis data set by using the PSU WRF-EnKF data assimilation system. This WRF-EnKF system was originally developed in Meng and Zhang (2008a, 2008b) and Zhang et al. (2009) but has since been further updated and applied in many subsequent studies including but not limited to analysis and prediction of rainfall (Bao et al., 2017; Qiu & Zhang, 2016), snowstorm (Saslo & Greybush, 2017) and thunderstorms (Zhang et al., 2018), and tropical cyclones (Weng & Zhang, 2012; Zhang et al., 2009; Zhang & Weng, 2015). The initial ensemble perturbations were generated with balanced perturbations randomly drawn from the “CV3” background error variance option of the WRF-3DVAR data assimilation system (Barker, 2005; Barker et al., 2004; Houtekamer et al., 2005) to create 40 initial ensemble members that are used to produce the first prior estimate at the very beginning of the reanalysis. In view of the use of a moderate ensemble size and the rather coarser resolution of available observations over the TP, the horizontal and vertical localization radii used for the sounding observations were 1,200 km and 15 model vertical levels, respectively; similar configurations were shown in Zhang et al. (2011) to have satisfactory performance. The covariance localization function (Gaspari & Cohn, 1999) is similar to many other regional EnKF studies (Ying et al., 2018). The EnKF analysis was performed every 6 hr (0000, 0600, 1200, and 1800 UTC). The covariance relaxation method was applied to prior perturbation following Zhang et al. (2004) with a relaxation coefficient of 0.8.

2.2. Forecast Model

Forecasts and downscale simulations were performed using the WRF model. Domain 01 (D01 in Figure 1) was used to generate ensemble analysis, with 114×69 horizontal grid points at a 30-km grid spacing and 60 vertical levels up to 10 hPa. Domain 02 (D02 in Figure 1), with 313×178 horizontal grid points at a grid spacing of 10 km, was utilized to perform downscale experiments driven by the mean of ensemble analysis over D01. The same physical schemes were used in the D01 and D02, including the WRF Double-Moment 6-class microphysics scheme (Lim & Hong, 2010), the longwave radiation scheme of Rapid Radiative Transfer Model for general circulation model applications (Iacono et al., 2008), the New Goddard shortwave radiation scheme (Chou & Suarez, 1999), the Monin-Obukhov similarity surface-layer scheme (Paulson, 1970), the

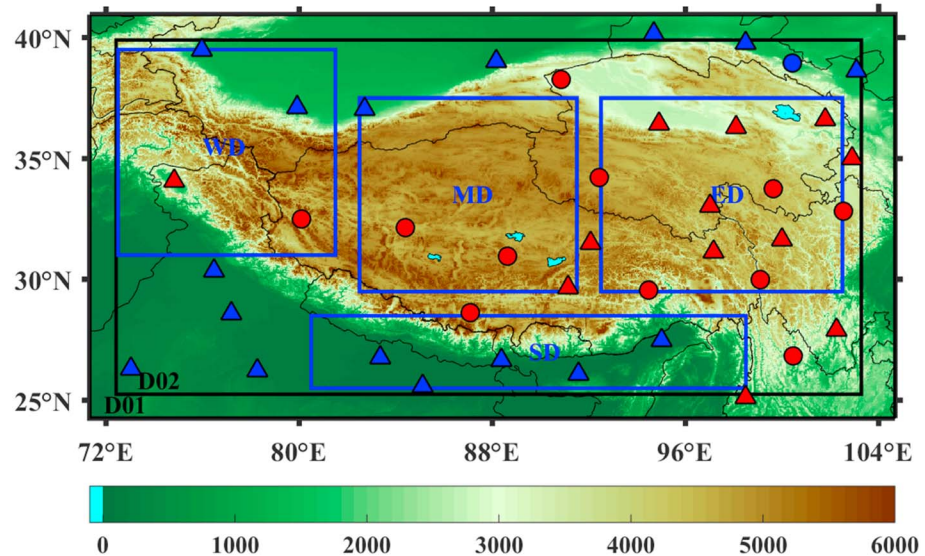


Figure 1. Configuration of the Weather Research and Forecasting-ensemble Kalman filter reanalysis domain (D01) and downscale reanalysis domain (D02) over the Tibetan Plateau. The triangles and dots represent the sounding sites of Global Telecommunications System that are assimilated in the model and the intensive sounding sites, respectively. Blue and red indicate sites below and above 1,500 m (observation record starts from 700 hPa), respectively. Verification domains (west domain, WD; middle domain, MD; east domain, ED; south domain, SD) of precipitation are shown as blue boxes inside D02. The shaded color indicates the terrain height in meters.

Noah land surface model, and the Yonsei State University boundary layer scheme (Hong et al., 2006). No cumulus parameterization scheme was used in either of the model domains (D01 and D02), which follows Chen et al. (2018). Note that the data assimilation method used by the WRF-EnKF system presented here is ensemble based, which is drastically different from those variational methods used for creating ERA-Interim and ERA5, the IFS Cycle 31r2 4DVAR (Berrisford et al., 2011) and IFS Cycle 41r2 4DVAR (Hersbach & Dee, 2016), respectively, besides their differences in model, resolution, and physics parameterization schemes. The spatial resolution, which is globally ~ 79 -km (~ 31 -km) horizontal grid spacing and 60 vertical levels up to 0.1 hPa (137 vertical levels up to 0.01 hPa) for ERA-Interim (ERA5), is lower than (comparable to) the 30-km horizontal resolution used in the WRF-EnKF system. The IFS 4DVAR system generated the ERA-Interim and ERA5 by assimilated the Global Telecommunications System (GTS) observations, satellite radiance data and others; however, the WRF-EnKF reanalysis only assimilated GTS observations in the current pilot evaluation study.

The initial and lateral boundary conditions (ICs and LBCs) for D01 were generated from ERA-Interim with a horizontal grid spacing of ~ 79 km. After a spin-up period from 1200 UTC 31 May to 0000 UTC 1 June 2015, the data assimilation cycles started from 0000 UTC 1 June and spanned the summer of 2015. The mean of 6-hr ensemble forecasts (EnKF_30_En6H) of the previous cycle was used as the new IC for the next data assimilation cycle.

Downscale simulations were performed at different grid spacings for different comparisons. ERA-I_30 and ERA5_30 at a 30-km grid spacing over D01 were interpolated from the original ERA-Interim (at a ~ 79 -km grid spacing) and ERA5 (at a ~ 31 -km grid spacing) reanalysis to compare with EnKF_30 (Table 1). The 12-hr downscale simulations (Table 1) using two-way nesting were driven by the reanalysis of ERA5_30 or ERA-I_30 or EnKF_30. Their coarser (nested) simulations at a 30-km (10-km) grid spacing over D01 (D02) are referred to as ERA-I_30_FCST, ERA5_30_FCST, and EnKF_30_FCST (ERA-I_10_FCST, ERA5_10_FCST, and EnKF_10_FCST). Consecutive deterministic forecasts were initiated each day at the four assimilation times during the summer of 2015, each integrated for 12 hr and with outputs saved every 3 hr. Within the four 12-hr forecasts of each day, every 3-hourly accumulated rainfall from hour 3 to 6 and the subsequent 3-hourly accumulated rainfall from hour 6 to 9 were concatenated to describe the diurnal evolution of precipitation in section 4.5. Different experiments over D01 and D02 are summarized in Table 1.

Table 1
A Summary of Data Assimilation Forecast and Downscale Experiments

Experiment name	Domain	Resolution (km)	Description
ERA-I_30	D01	30	Interpolated ERA-Interim reanalysis to 30-km grid spacing
ERA5_30	D01	30	Interpolated ERA5 reanalysis to 30-km grid spacing
EnKF_30	D01	30	Mean of the EnKF ensemble analysis
ERA-I_10	D02	10	Interpolated from ERA-I_30 to 10 km grid spacing
ERA5_10	D02	10	Interpolated from ERA5_30 to 10 km grid spacing
EnKF_10	D02	10	Interpolated from EnKF_30 to 10 km grid spacing
ERA-I_30_FCST	D01	30	Deterministic forecast from ERA-I_30
ERA5_30_FCST	D01	30	Deterministic forecast from ERA5_30
EnKF_30_FCST	D01	30	Deterministic forecast from EnKF_30
ERA-I_10_FCST	D02	10	Deterministic forecast from ERA-I_10
ERA5_10_FCST	D02	10	Deterministic forecast from ERA5_10
EnKF_10_FCST	D02	10	Deterministic forecast from EnKF_10
ERA-I_30_6H	D01	30	6-hr forecast result from ERA-I_30_FCST
ERA5_30_6H	D01	30	6-hr forecast result from ERA-5_30_FCST
EnKF_30_6H	D01	30	6-hr forecast result from EnKF_30_FCST
ERA-I_30_12H	D01	30	12-hr forecast result from ERA-I_30_FCST
ERA5_30_12H	D01	30	12-hr forecast result from ERA-5_30_FCST
EnKF_30_12H	D01	30	12-hr forecast result from EnKF_30_FCST
ERA-I_10_6H	D02	10	6-hr forecast result from ERA-I_10_FCST
ERA5_10_6H	D02	10	6-hr forecast result from ERA-5_10_FCST
EnKF_10_6H	D02	10	6-hr forecast result from EnKF_10_FCST
ERA-I_10_12H	D02	10	12-hr forecast result from ERA-I_10_FCST
ERA5_10_12H	D02	10	12-hr forecast result from ERA-5_10_FCST
EnKF_10_12H	D02	10	12-hr forecast result from EnKF_10_FCST
ERA-I_79_ORIG	Global	79	Original forecasts from ERA-Interim data set
ERA5_31_ORIG	Global	31	Original forecasts from ERA5 data set

Note. EnKFs = ensemble Kalman filter; ERA5 = fifth European Centre for Medium-Range Weather Forecasts Reanalysis.

2.3. Observations

The pilot reanalysis data sets evaluated in this study were produced by EnKF over D01 that assimilated conventional observations available from GTS platform every 6 hr. The assimilated GTS data set includes surface observation (SYNOP), radiosonde observation (TEMP), satellite wind (SATOBS), aerodrome routine meteorological report (METAR), automated aircraft report (AMDAR), satellite remote upper-air sounding (SATEM), upper-wind report (PILOT), and space-based GPS refractivity observation (GPSRF). The standard GTS soundings assimilated in all reanalyses, which are denoted by the triangles in Figure 1, are only independent for verifying the 6- to 12-hr WRF forecasts. Dots that represent the intensive radiosonde sites from TIPEX-III, which are not assimilated in this study, are independent observations for verifying both the (re) analysis and the subsequent 6- to 12-hr forecasts. To evaluate the reanalysis quality over the TP, independent soundings only at sites over high plateaus with elevation above 1,500 m (shown by red color in Figure 1) were collected to verify the reanalyses (against red dots) and subsequent forecasts (against red triangles and red dots).

The Advanced TIROS Operational Sounder Level 2 (ATOVS2) satellite-retrieved sounding observations (Bormann & Bauer, 2010; Li et al., 2000) were also used to evaluate the specific humidity and temperature of the reanalyses and forecasts. Radiance observations primarily from two series of satellites, NOAA and Metop, were used to develop the ATOVS2 data sets. Retrieved from measurements of the Advanced TIROS Operational Vertical Sounder, ATOVS2 global data sets contain vertical profile of temperature at 40 pressure levels from 10 to 1,000 hPa and specific humidity at 15 pressure levels from 300 to 1,000 hPa. Merged surface-Climatology Prediction Center MORPHed (CMORPH) rainfall observations (Joyce et al., 2004; Qi et al., 2018; Shen et al., 2014) were used to evaluate the simulated rainfall over the TP.

3. Evaluation Metrics

The reanalysis and subsequent forecasts were evaluated by calculating the mean bias and root-mean-square errors (RMSEs). The mean bias was defined as

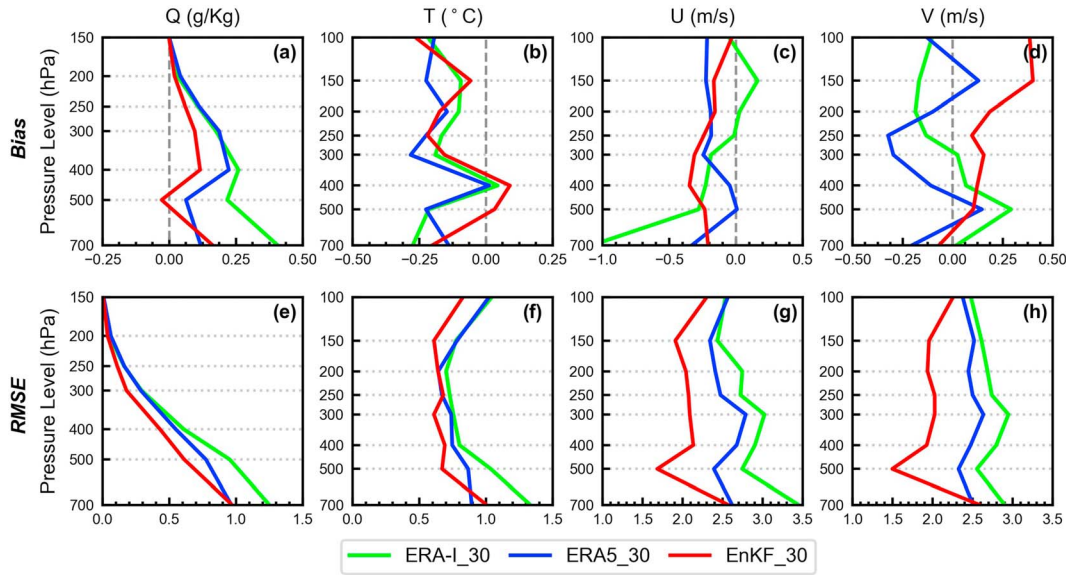


Figure 2. Vertical profiles of mean bias (a–d) and root-mean-square error (RMSE; e–h) for ERA-Interim reanalysis (green: ERA-I_30), ERA5 reanalysis (blue: ERA5_30), and the Weather Research and Forecasting-ensemble Kalman filter reanalysis (red: EnKF_30) verified at the Global Telecommunications System sounding sites (12 red triangles in Figure 1) for specific humidity (a and e), temperature (b and f), U wind (c and g), and V (d and h) wind over D01 during the summer season of 2015.

$$\text{Bias} = \frac{1}{n} \sum_{i=1}^n (M_i - O_i) \quad (1)$$

where M_i and O_i denote the model simulated value and observation at the i th ($i = 1, 2, 3, \dots, n$) site, respectively. All the M_i were interpolated from model grid to observation sites on the pressure level by the bilinear interpolation algorithm. RMSE was defined as

$$\text{RMSE} = \sqrt{\frac{1}{n} \sum_{i=1}^n (M_i - O_i)^2} \quad (2)$$

The adjusted ensemble spread following Houtekamer et al. (2005) was defined as

$$\text{SPRD} = \sqrt{\frac{1}{N-1} \sum_{i=1}^N (f_i - \bar{f})^2 + \sigma_o^2} \quad (3)$$

where f_i and \bar{f} represent the i th ($i = 1, 2, 3, \dots, N$) ensemble member and the ensemble mean, respectively, and σ_o^2 is the observational error variance. Consistent with the innovation statistics as in (Parrish & Derber, 1992) commonly used for examining the consistency between ensemble spread and root-mean difference to observations, the prior ensemble can be regarded as generally reasonable when the prior RMSE is comparable to the square root of the sum of background error variance and observation error variance (SPRD hereinafter) following Meng and Zhang (2008b).

4. Results

4.1. Evaluation of Overall RMSE and Bias Against Sounding Observations

The WRF-EnKF, ERA-Interim, and ERA5 reanalysis are compared in this section. All the bias and RMSE showed in this section were calculated based on independent sounding observations at elevations higher than 1,500 m (observation record starts from 700 hPa), except for those shown in Figure 2, which used the sounding observations that were assimilated. Figure 2 shows the RMSE of EnKF_30 is smaller than those of ERA-I_30 and ERA5_30, especially in terms of specific humidity (Q) and of horizontal winds (U and V). In general, the bias of temperature (T) and horizontal winds are similar in these three reanalyses, while the EnKF_30 Q shows considerably smaller bias compared to the two global reanalyses, particular to ERA-

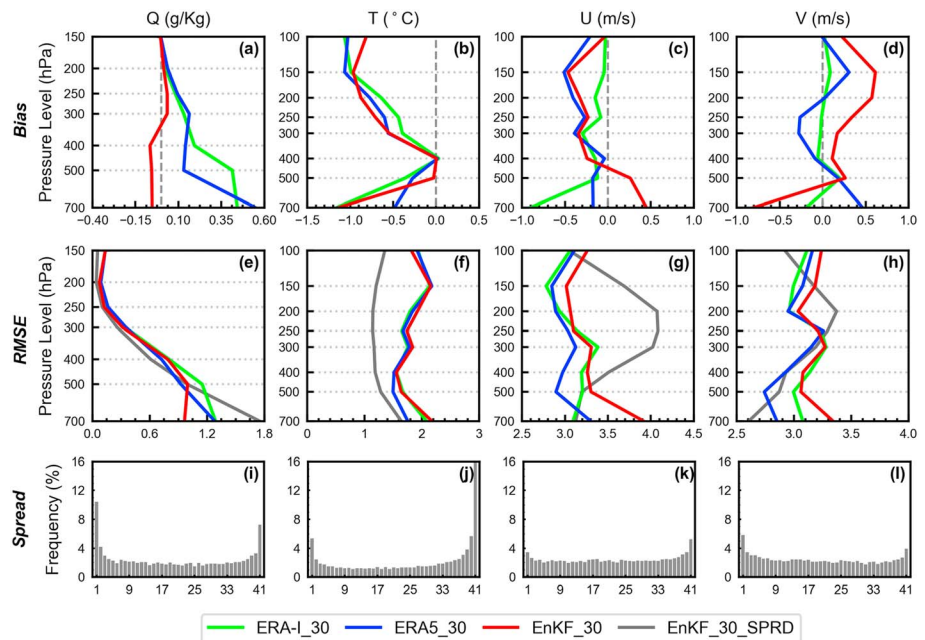


Figure 3. As in Figure 2 but verified at the intensive sounding sites (11 red dots in Figure 1) for the ERA-I_30 (green), ERA5_30 (blue), and EnKF_30 (red) reanalyses. Grey line displays the spread of the Weather Research and Forecasting-ensemble Kalman filter reanalysis (EnKF_30_SPRD). (i–l) The rank histogram of posterior ensemble for Q , T , U , and V . The y coordinate denotes the relative frequency of the verifying observation; the x coordinate denotes the bins formed by the ensemble.

I_30. The results implied that this pilot EnKF data assimilation system worked effectively even though only the GTS observations were assimilated. Nevertheless, we note that the EnKF_30 V wind had a slightly larger bias than ERA-I_30 and ERA5_30 at the upper to middle levels, implying that there is still room for improving the WRF-EnKF ensemble-based reanalysis configurations, along with future inclusion of other observations including those from the satellites.

The mean bias (Figures 3a–3d) and RMSE (Figures 3e–3h) of Q , T , U , and V were calculated using the independent sounding observations (red dots in Figure 1) during the summer of 2015. Figures 3a and 3e show that the EnKF_30 had apparent improvement in Q at all vertical levels when compared to ERA-I_30 and ERA5_30. The positive bias (Figure 3a) of ERA-I_30 and ERA5_30 reached up to 0.4 and 0.5 g/kg at 700 hPa, while the bias of EnKF_30 was close to the zero line with a negative value less than 0.1 g/kg. Although the ERA5_30 bias is smaller than ERA-I_30 near 500 hPa, it still is larger than the EnKF_30 bias. Consistent with the bias, the RMSE of Q (Figure 3e), which was comparable with the ensemble spread underestimated shown in Figure 3i, was also smaller than those of ERA-I_30 and ERA5_30, except at the pressure levels from 400 to 500 hPa in ERA5_30. Generally speaking, comparable performance (Figures 3b and 3f) was observed in T between the three reanalyses except that EnKF_30 had a slightly larger error than ERA-I_30 in the middle troposphere and ERA5_30 in the lower levels. The rank histogram indicated the ensemble spread was underestimated in T . Although it is beyond the scope of this study, it is foreseeable in the future we can test different relaxation coefficient or using adaptive covariance inflation methods (Yue & Zhang, 2015) in EnKF to have better spread of specific humidity and temperature successively while retaining the advantage in the accuracy of the analysis. The bias of U wind (Figure 3c) of EnKF_30 was slightly smaller than that of ERA5_30 excluding at near surface, but ERA-I_30 displaying a smallest bias at upper levels and a larger bias at lower levels. The RMSE of U wind (Figure 3g) of EnKF_30 was larger than that of ERA-I_30 and ERA5_30, and the ERA5_30 showed the smallest RMSE. The spread of U wind was reasonable based on the flat rank histogram (Figure 3k); however, its vertical profile was far away from the RMSE of EnKF_30 at middle levels, which was likely due to the larger observation error variance (~ 9 m/s) between 150 and 300 hPa according to equation (3). EnKF_30 displayed a larger bias (Figure 3d) compared to ERA-I_30 and ERA5_30 for V wind at most levels. V wind (Figure 3h) showed an analogous feature to U wind in terms of the RMSE for EnKF_30. However, different from the U wind, the V

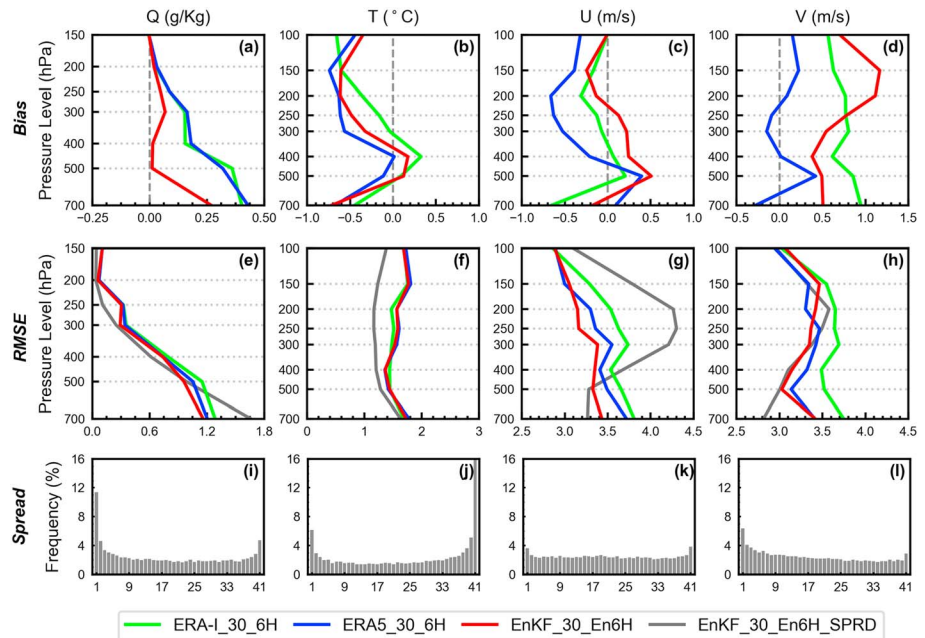


Figure 4. As in Figure 3 but verified at the independent sounding sites (12 red triangles and 11 red dots in Figure 1) for 6-hr forecasts driven by three reanalyses. Grey line displays the spread of ensemble forecast (EnKF_30_En6H_SPRD). The rank histogram of 6-hr ensemble forecast shows in bottom panels (i–l). RMSE = root-mean-square error.

wind of EnKF_30 showed a reasonable vertical spread but with a slight deficiency (Figure 3k) compared to its RMSE.

Further improvements were observed in the reanalysis initiated short-term forecast (and subsequent down-scaling) than in the analysis (Figure 3) with the WRF-EnKF. The mean of 6-hr ensemble forecasts (EnKF_30_En6H) from the posterior ensemble members showed notable improvement relative to that from ERA-I_30 and ERA5_30 (ERA-I_30_6H and ERA5_30_6H), particularly for specific humidity at all vertical levels (Figures 4a and 4e). The rank histogram of EnKF_30_En6H (Figure 4i) was similar to Figure 3i, but the ensemble vertical spread (Figure 4e) was closer to RMSE than that of Figure 3e. The mean bias (Figure 4b) of T generally showed similar performance between EnKF_30_En6H and ERA-I_30_6H, with a smaller bias of EnKF_30_En6H than that of ERA-I_30_6H near 400 hPa and above 150 hPa. The T bias was larger than EnKF_30_En6H and ERA-I_30_6H in term of ERA5_30_6H. The temperature RMSE (Figure 4f) had an even smaller difference between the three forecasts with respect to that difference in Figure 3f, and the temperature spread (Figure 4f) of EnKF_30_En6H underestimated based on Figure 4j was closer to its RMSE relative to the vertical spread of EnKF_30 (Figure 3f). The bias of U wind exhibited an analogous shape in the EnKF_30_En6H and ERA-I_30_6H (Figure 4c) and was smaller than that of ERA5_30_6H at middle-to-upper levels. The bias of V wind (Figure 4d) of EnKF_30_En6H was smaller at lower to middle levels and larger at upper levels compared to ERA-I_30_6H, while the ERA5_30_6H showed the smallest bias than the others. The wind RMSE of EnKF_30_En6H (Figures 4g and 4h) was consistently smaller than that of ERA5_30_6H at lower-to-middle levels and ERA-I_30_6H with a maximum difference of ~ 0.5 m/s, even though the wind of EnKF_30 was worse than ERA-I_30 and ERA5_30 in Figures 3g and 3h. This is likely due to the advantage of the EnKF-based reanalysis using flow-dependent error covariance from the short-term ensemble forecasts with a higher-resolution, nonhydrostatic regional model, rather than due to the ensemble spread, which showed more flat rank histogram than that of posterior ensemble (Figure 3k) for U wind and a positive bias (Figure 4l) for V wind. Overall, the EnKF_30_En6H simulations outperform the other two 6-hr simulations, which were initialized with ERA-Interim and ERA5 reanalysis.

4.2. Evaluation of Specific Humidity Against Satellite Observation

The performances of EnKF_30 and ERA-I_30 were evaluated against the ATOVSL2 observations (Ahn et al., 2003; Bormann & Bauer, 2010; Li et al., 2000) from NOAA19, MetopA, and MetopB satellites for temperature

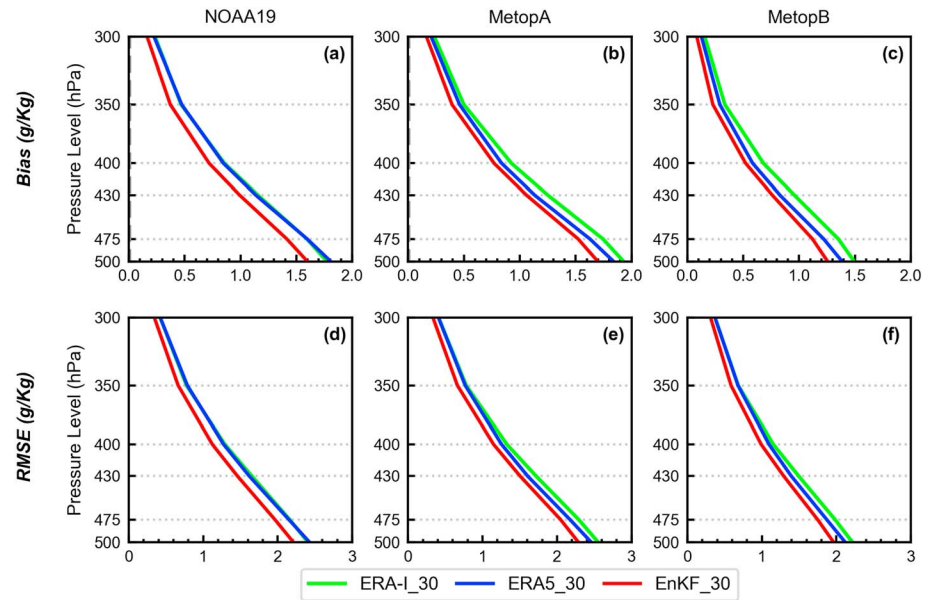


Figure 5. As in Figure 2 but verified against ATOVSL2 NOAA19 (a and d), MetopA (b and e), and MetopB (c and f) satellite-retrieved observations for the specific humidity of three reanalyses over D01. Verification times are 06 UTC and 18 UTC for NOAA19 and 06 UTC and 12 UTC for MetopA and MetopB. RMSE = root-mean-square error.

and specific humidity. Note that some of the radiances used to derive the satellite-retrieved ATOVSL2 observations have been assimilated for the ERA-Interim and ERA5 reanalyses (that initiated ERA-I_30 and ERA5_30) but none was used for the WRF-EnKF (for initiating EnKF_30). Nevertheless, regardless of which satellite observations were compared against, EnKF_30 had smaller bias and RMSE in specific humidity than those of ERA-I_30 and ERA5_30, indicating that the specific humidity of EnKF_30 over the TP was more reliable and accurate than that of ERA-I_30 and ERA5_30 (Figure 5) consistent with the verification against sounding sites as shown in Figure 3. Consistently, smaller biases and RMSE of specific humidity were also observed in terms of 6-hr forecasts (Figure 6) in EnKF_30_En6H relative to ERA-I_30_6H and ERA5_30_6H except that the ERA5_30_6H exhibited a commensurate bias at middle-to-upper levels when

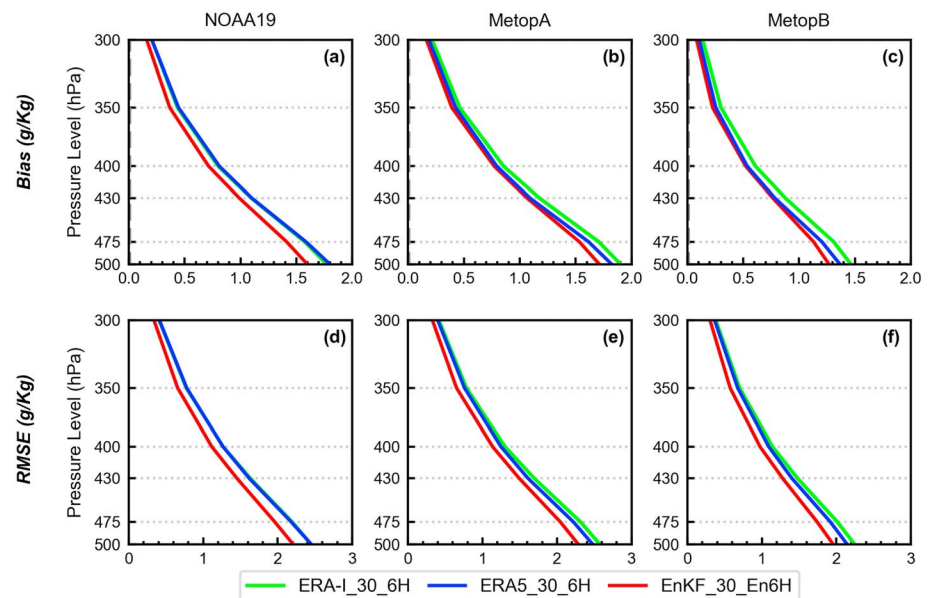


Figure 6. As in Figure 5 but for the 6-hr Weather Research and Forecasting forecasts. RMSE = root-mean-square error.

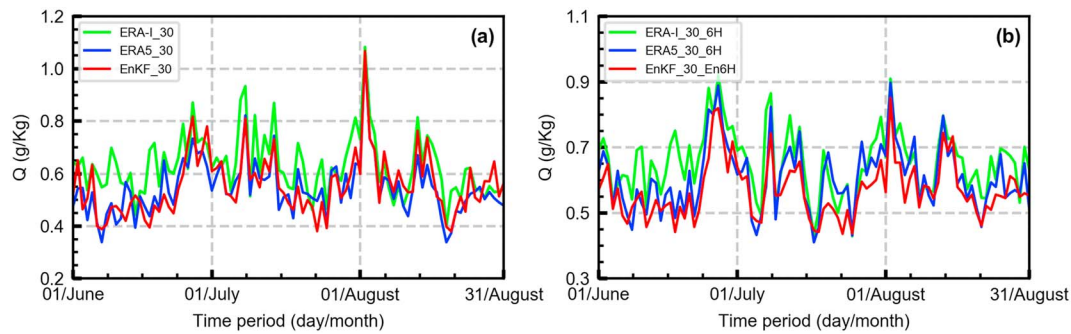


Figure 7. Time evolution of the vertically averaged (from 300 to 700 hPa) root-mean-square error of specific humidity for (a) the three reanalyses and (b) the sequent 6-hr Weather Research and Forecasting forecasts initialized from respective reanalyses during the summer season of 2015. Root-mean-square error is the average at 00, 06, 12, and 18 UTC for each day.

compared against MetopA/MetopB. In addition, the bias and RMSE (Figures 5 and 6) based on MetopB observations were the smallest, followed by that of MetopA and NOAA19, probably because of different accuracy of different satellite observations, but more detailed analysis is out of scope for this work.

In summary, the independent sounding and satellite observations demonstrated that the EnKF_30 improved notably over ERA-Interim and ERA5 in specific humidity estimation and subsequent forecasts. The improved moisture analysis will have significant implications in the precipitation analysis, and the water cycles over this region, which is one of the primary objectives in developing a regional reanalysis data set as the eventual goal. As for the verification of temperature with ATOVSL2 observation, the bias and RMSE showed comparable values for three reanalysis and forecast (not shown).

4.3. Evaluation of Specific Humidity in Spatial and Temporal Distribution

As the WRF-EnKF pilot reanalysis tended to show a more accurate description for the key components of the water cycles over the TP, the daily evolution of the vertically averaged RMSE of Q (Figure 7) from 300 to 700 hPa is further examined against the same soundings used in Figures 3 and 4. The ERA5_30 RMSE was smaller than that of ERA-I_30 in most days during summer, especially in June and July (Figure 7a). Compared with ERA5_30, the EnKF_30 RMSE showed a favorable performance. Furthermore, the 6-hr ensemble forecast initiated from the EnKF_30 showed smaller RMSE than that from ERA-I_30_6H and most days of ERA5_30_6H (Figure 7b), indicating again the advantages of the EnKF_30 in terms of specific humidity.

Figure 8 displays the horizontal distributions of vertically averaged error of specific humidity at verification sites (red markers in Figure 1) that have observations starting from 700 hPa. The ERA5 experiment (Figure 8b) particularly over the sites of the eastern TP had a slightly smaller bias than the ERA-Interim experiment (Figure 8a) with the largest positive value of ~ 0.3 g/Kg. However, the EnKF experiment (Figure 8c) displayed the smallest bias over most sites, which was consistent with Figure 3a. Using more verifiable sites, the 6-hr forecasts of ERA-I_30 and ERA5_30 showed larger biases (Figures 8d and 8e) with the biases greater than 0.1 g/kg at most sites over the TP. The EnKF_En6H bias (Figure 8f) of specific humidity was less than 0.1 g/Kg over most sites, thus closer to the observations more significantly than ERA-I_30 and ERA5_30 forecasts, except for several sites on the southeast of TP and India. The RMSE (Figures 8g–8l) distribution characterizations of specific humidity of EnKF experiment were analogous to that of the bias in Figures 8a–8f. Overall, the WRF-EnKF reanalysis data sets provided more accurate spatiotemporal features of specific humidity than ERA-Interim and ERA5.

4.4. Evaluation of Downscale Data Sets

Dynamical downscaling was performed to produce high-resolution model data sets through running 6- and 12-hr deterministic forecast at a 10-km grid spacing from ERA-I_30, ERA5_30, and EnKF_30. The 10-km downscale experiments were verified with the same observations as used to verify reanalyses and their forecasts in Figures 3 and 4. In general, the downscale experiment of the EnKF_30 was more accurate than that of the ERA-I_30 but comparable to ERA5_30.

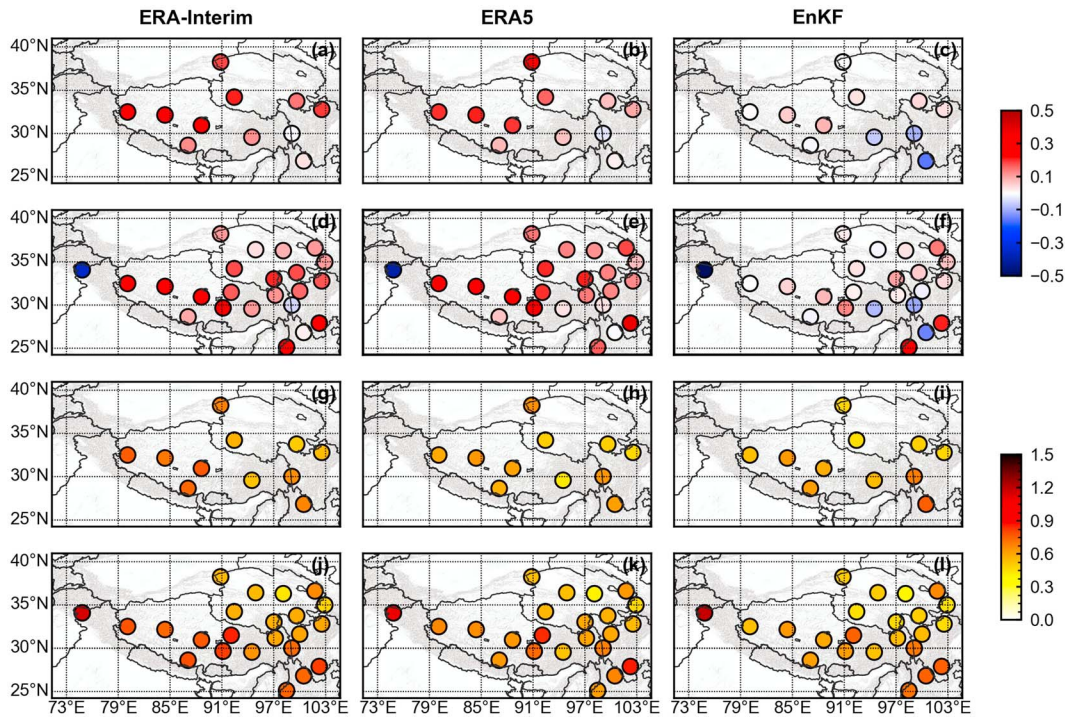


Figure 8. Spatial distribution of the vertically averaged (from 300 to 700 hPa) bias (a–f) and root-mean square error (g–l) for specific humidity (g/kg) during the summer season of 2015. (a–c and g–i) Reanalysis fields and (d–f and j–l) 6-hr forecasts for ERA-Interim (a, d, g, and j), fifth European Centre for Medium-Range Weather Forecasts Reanalysis (ERA5; b, e, h, and k), and Weather Research and Forecasting-ensemble Kalman filter (EnKF; c, f, i, and l). The same verified sounding sites and units as in Figures 3 and 4 for the bias and root-mean-square error of specific humidity.

The bias and RMSE of the specific humidity of EnKF_10 (Figures 9a and 9e), which was interpolated into a 10-km grid spacing from EnKF_30, was smaller than that of ERA-I_10 and ERA5_10 as the reanalyses at 30-km grid spacing. The EnKF_10 forecasts (EnKF_10_6H and EnKF_10_12H) biases of specific humidity were positive except near 400 hPa and smaller than that of ERA-I_10_6H and ERA-I_10_12H (ERA5_10_6H and ERA5_10_12H). This might result in too strong predicted precipitation, but the EnKF_10 forecasts were much closer to the observed precipitation than the WRF forecasts downscaled from ERA-I_30 and ERA5_30. For the RMSE of the forecasts, The EnKF_10_6H and EnKF_10_12H showed a slightly larger error than ERA5_10_6H and ERA5_10_12H but smaller than ERA-I_10_6H and ERA-I_10_12H. The three downscale experiments had comparable temperature bias (Figure 9b) at the corresponding times, but the ERA-I_10 and ERA5_10 downscale had a smaller RMSE (Figure 9f) than that of EnKF_10 downscale at middle levels (from 200 to 400 hPa). For wind, bias and RMSE of ERA-Interim experiments (Figures 9c and 9d, and 9g and 9h) grown faster along forecast times than those of the ERA5 and EnKF experiments and became greater after 6 hr, except that the bias of *U* wind of three experiments was of comparable magnitudes (Figure 9c). Additionally, the wind bias of ERA5_10 and subsequent forecasts were the smallest, followed by the EnKF_10 and ERA-I_10 simulations. ERA5_10_6H and ERA5_10_12H exhibited smaller magnitude for wind RMSE than EnKF_10_6H and EnKF_10_12H although the EnKF_30_En6H showed a smaller RMSE compared to ERA5_30_6H. It was found that ERA5 downscale at 10-km grid spacing displayed an advantage than the others, followed by EnKF and ERA-Interim downscale simulations. The compared experiments (not shown) at the 30-km horizontal resolution displayed a similar performance to the downscale experiments at the 10-km horizontal resolution.

4.5. Evaluation of Diurnal Precipitation

In view of the more apparent and consistent improvement in specific humidity, further verification of precipitation using the 10-km downscale experiments over the D02 was performed. Three-hourly accumulated precipitation from surface-CMORPH observations and downscale experiments are shown in Figure 10. According to the observations (Figures 10a–10h), precipitation mainly occurred along the southern edge

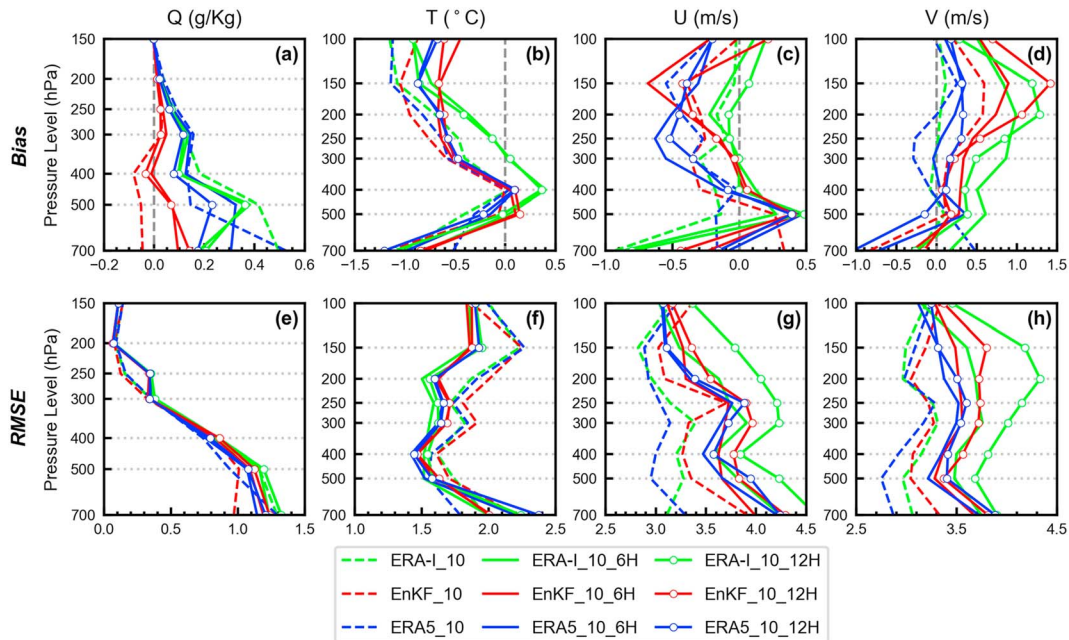


Figure 9. As in Figure 2 but verified against independent sounding observations over D02 for the reanalysis as well as the 6- and 12-hr Weather Research and Forecasting forecasts initialized from ERA-I_30, ERA5_30, and EnKF_30. RMSE = root-mean-square error.

of TP during summer, which was closely related to the lifting effects of the Himalaya mountains. The averaged extreme value of accumulated precipitation within 3 hr at 0800 LST (local standard time) reached ~11 mm over the south TP slope (subdomain, SD) and 1-3 mm over the eastern TP and India (eastern domain, ED). Notably, there were some local scattered precipitation near the lakes (e.g., Zhari Namco, Selin Co, and Nam Co, located on the middle domain [MD] with cyan color in Figure 1) mostly located at the middle TP (MD), especially at 1100, 2000, and 2300 LST. The accumulated precipitation increased from 0200 LST, peaking at 0800 LST, then decreased until 1400 LST, followed by increasing again to the second peak at 2000 LST.

The rainfall forecast of the ERA-I_30 downscale experiment (Figures 10i–10p) showed a similar distribution and diurnal variation patterns as the surface-CMORPH observations. However, the simulated precipitation was considerably larger along the southern edge of the TP and over the main body of TP (Figures 10i–10k and 10n–10p). Compared with ERA-I_10_FCST, despite the rainfall from ERA5_10_FCST (Figures 10q–10x) showed apparent improvement in term of precipitation intensity, which showed the maximum rainfall reduced from 40 to 25 mm within 3 hr along the southern edge of TP, ERA5_10_FCST precipitation were still more heavier than observation. The precipitation forecast from the EnKF_30 downscaling experiment (Figures 10I–10VIII), however, simulated more reasonable precipitation including a better precipitation magnitude and less spurious rainfall over the TP. It was found that the three reanalyses simulated the best precipitation forecasts in daytime from 0800 LST to 1700 LST and the worst nighttime rainfall from 2000 LST to 0500 LST. The smallest precipitation bias was at 1400 LST in EnKF_10_FCST and the largest precipitation bias appeared at 2000 LST and 2300 LST in ERA-I_10_FCST that could also be seen in Figure 11. The performance of reanalyses in different times of the day could be captured from the variation of rain rates (Figure 11), which were calculated and spliced from the forecasts driven by the reanalyses at 0800 LST, 1400 LST, 2000 LST, and 0200 LST. It indicates that the reanalyses (ERA-Interim, ERA5 and WRF-EnKF) from 0200 LST to 0800 LST showed the best rainfall forecasts than that from 1400 LST to 2000 LST while they showed the largest rainfall bias in their forecasts in the night. Consequently, three reanalyses should be improved during the night particular for rainfall forecasts of 2000 LST and 2300 LST in future, even though the WRF-EnKF initiated forecasts have improved much compared to ERA-Interim and ERA5 forecasts. Besides the data assimilation, the differences between the ERA reanalyses and the WRF-EnKF analysis could also be partially contributed by the different physics schemes used in the ERA forecast models and the WRF model. The relative contributions of data assimilation and model configurations to the

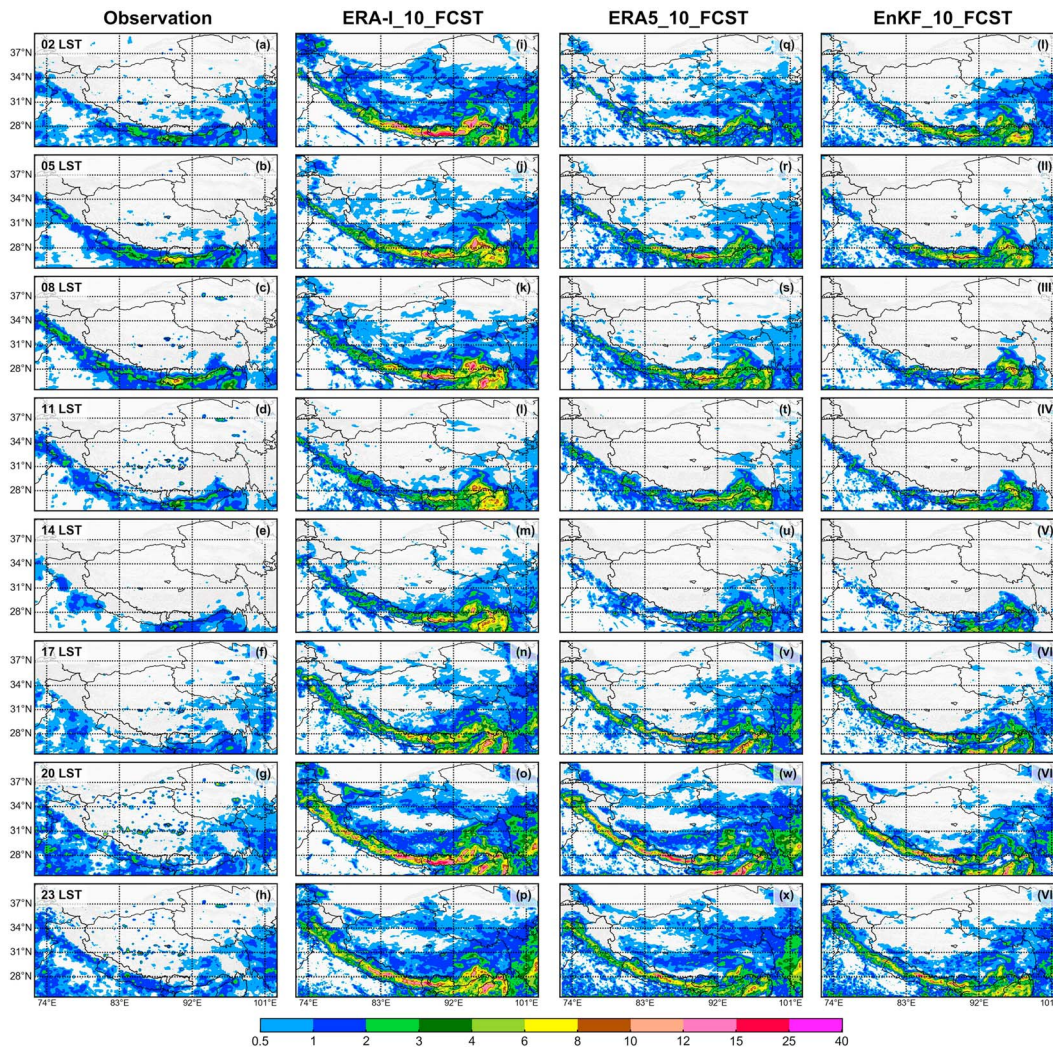


Figure 10. Spatial distributions of 3-hourly accumulated rainfall from different downscale forecasts (units: mm). (a–h) Observation; (i–p) ERA-I_10_FCST downscaled ERA-I_30; (q–x) ERA5_10_FCST downscaled ERA5_30; and (I–VIII) EnKF_10_FCST downscaled EnKF_30 at the 10-km horizontal grid spacing.

improvement deserve future investigations. The precipitation variation (not shown) from downscale experiments over D01 at the 30-km grid spacing (ERA-I_30_FCST or ERA5_30_FCST or EnKF_30_FCST) had an analogous shape, but a weaker intensity than the precipitation of the 10-km grid spacing (ERA-I_10_FCST or ERA5_10_FCST or EnKF_10_FCST), which can also be seen in Figure 11. This was likely due to better resolvability of mesoscale precipitation at the finescale grid (10 km) using fully explicit precipitation than that at the coarse-grid (30-km) domain that relies heavily on cumulus parameterizations.

Diurnal cycles of hourly rain rate over D02 from observation, three reanalysis simulations at 10- and 30-km grid spacing, ERA5_31_ORIG, and ERA-I_79_ORIG were compared in Figure 11. ERA-I_79_ORIG (bold purple) not only overestimated the precipitation with an averaged rain rate of ~ 0.34 mm/hr but also showed an erroneous diurnal cycle of rainfall with a maximum value of ~ 0.38 mm/hr at 1400 LST and a minimum value of ~ 0.27 mm/hr at 2000 LST. In contrast, the ERA5_31_ORIG (bold magenta) rainfall showed a reasonable diurnal variation but with a averaged rain rate of ~ 0.21 mm/hr that was larger than the CMORPH observational analysis, while there was still a 3-hr delay in the diurnal precipitation peak compared to CMORPH. ERA-I_30_FCST and ERA-I_10_FCST (green lines) had a better diurnal cycle of rain rate than that of ERA-I_79_ORIG though still with a larger value than the observation with the minimum of ~ 0.2 mm/hr and the maximum of ~ 0.44 mm/hr. The relatively better rain rates from ERA5_30_FCST and ERA5_10_FCST (blue lines) correctly caught the diurnal variation in comparison to ERA5_31_ORIG.

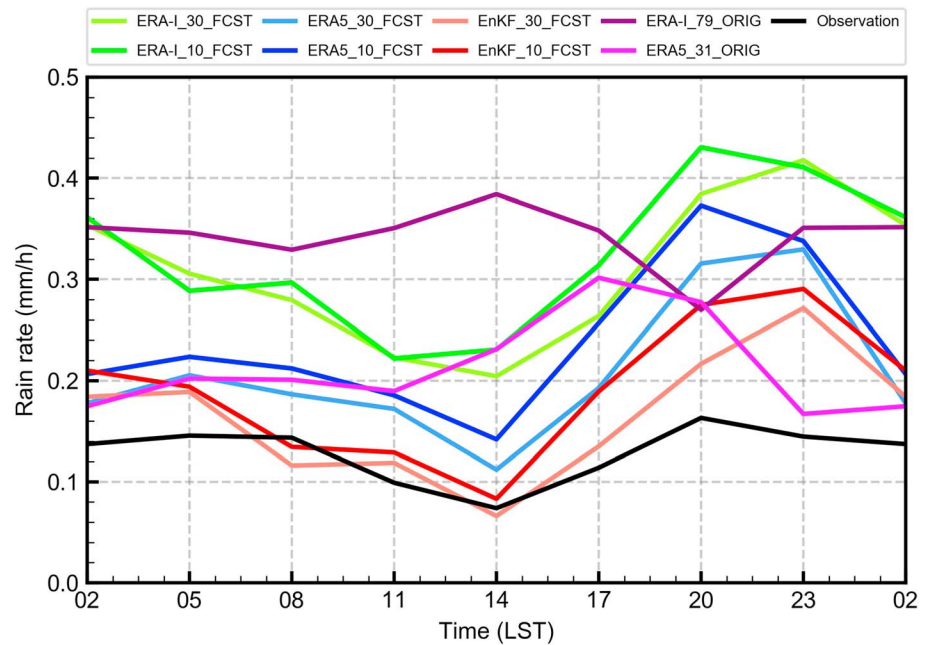


Figure 11. Diurnal cycles of D02-averaged hourly rainfall from different downscaled forecasts. The black line represents observation, the bold (light) green line represents ERA-I_10_FCST (ERA-I_30_FCST), the bold (light) blue line represents ERA5_10_FCST (ERA5_30_FCST), the bold (light) red line represents EnKF_10_FCST (EnKF_30_FCST), and the magenta and purple lines represent the rain rate of the original forecasts (ERA-5_31_ORIG and ERA-I_79_ORIG) from fifth European Centre for Medium-Range Weather Forecasts Reanalysis (ERA5) and ERA-Interim at ~31 and ~79 km grid spacing respectively. The x coordinate shows the time using local standard time. LST = local standard time.

Furthermore, the ERA5 simulations were closer to satellite-observed rain rates than ERA-Interim simulations. The rain rates (red lines) of EnKF_30_FCST and EnKF_10_FCST had similar diurnal variation pattern and comparable rainfall intensity to the observations, except that the evening peak was slightly overestimated. The largest difference between observation and three downscale experiments was ~0.27 mm/hr at 2000 LST in ERA-Interim experiment, followed by ERA5 and EnKF experiments. These findings suggest that the prototype WRF-EnKF reanalysis had considerable advantages in simulating diurnal precipitation over the TP in comparison to ERA-Interim and ERA5.

Different features in the diurnal variations of hourly rain rate were observed over the four TP subregions (Figure 12). The West Domain (WD) region showed a similar diurnal cycle pattern to the whole D02 domain, in which ERA-I_30_FCST and ERA-I_10_FCST showed notable moist bias, while EnKF-based forecasts (EnKF_30_FCST and EnKF_10_FCST) were much smaller. The EnKF-based downscale rainfall over WD had a comparable performance to ERA5_31_ORIG, ERA5_30_FCST, and ERA5_10_FCST evaluated against CMORPH observation; the latter had a better fit from 0500 LST to 1400 LST, while the former had a better fit from 1400 LST to 2000 LST. Over the MD of the TP region, the EnKF-based forecasts better captured the diurnal cycle of precipitation than the ERA-Interim (ERA5) forecasts at the 79- (31-), 30-, 10-km grid spacing due to the reducing of spurious precipitation. In contrast, ERA5_31_ORIG and the rain rates of ERA5 downscale experiments over MD was better than those downscaled from ERA-Interim. The ED had a local rainfall center over the TP with a mean hourly rain rate of ~0.1 mm/hr. Compared with ERA-Interim (ERA-I_30_FCST, ERA-I_10_FCST, and ERA-I_79_ORIG) and ERA5 precipitation (ERA5_30_FCST, ERA5_10_FCST, and ERA5_31_ORIG), the EnKF-based precipitation simulation well captured the shape and scale of diurnal cycle over ED, except that its rainfall bias were larger than that of observation and ERA5_31_ORIG during the night. This improvement depended on the more accurate WRF-EnKF reanalysis as clearly shown by the bias and RMSE in Figure 8 over the ED area. In term of ERA-I_30 downscaled rainfall products, ERA5_30_FCST and ERA5_10_FCST rainfall over ED displayed a comparable diurnal cycle and slightly smaller bias, while ERA5_31_ORIG had an apparent smaller rainfall bias.

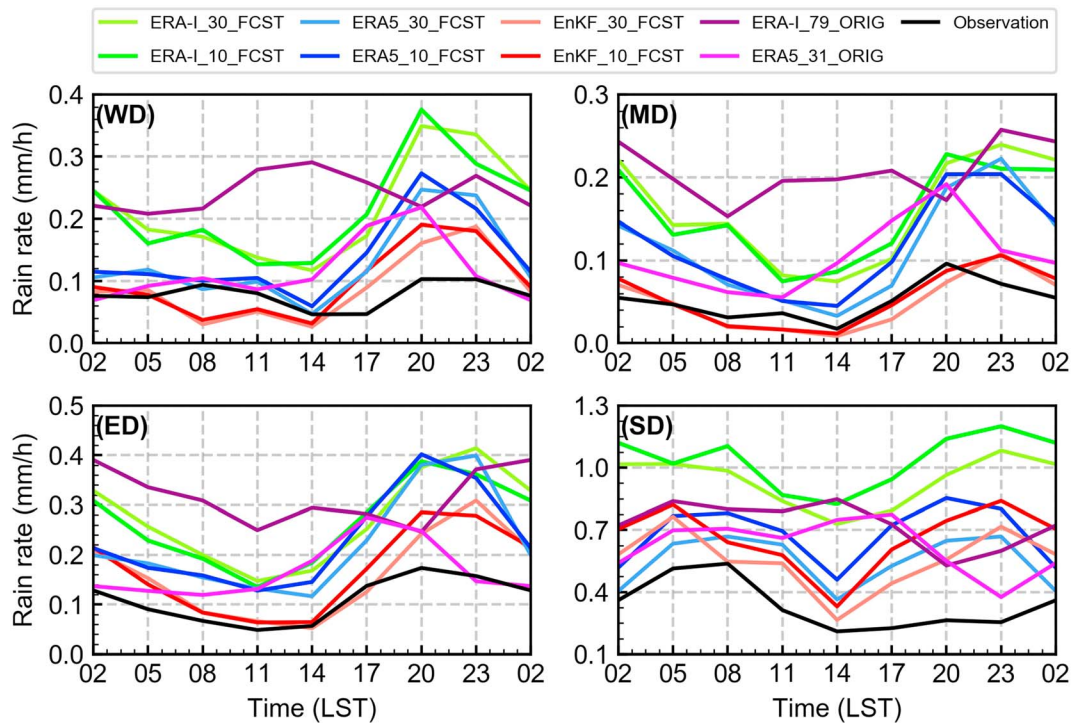


Figure 12. As in Figure 11 but evaluated over the blue domains (west domain, WD; middle domain, MD; east domain, ED; south domain, SD) as shown in Figure 1.

The primary precipitation center of the TP was located over the south domain (SD). Rainfall simulation over this region was still a challenge for most current numerical weather prediction models (Feng & Zhou, 2012; Maussion et al., 2011; Maussion et al., 2014; Wang & Zeng, 2012), likely due to its complex terrains and related complicated dynamic and thermodynamic processes (Lin et al., 2018; Zhou et al., 2018). The biases of the EnKF-based forecast rainfall (red lines) were much smaller than those of the ERA-Interim forecasts (green and purple lines) over SD during the daytime, primarily due to the better moisture in the WRF-EnKF reanalysis as discussed in Figure 10. In term of ERA5 simulations (blue and magenta lines), the rain rates of EnKF-based forecast showed an analogous performance with smaller bias in the day and larger bias in the night. Overall, the rainfall diurnal cycle and intensity from downscaled forecasts initialized with the WRF-EnKF reanalysis showed distinct advantages in comparison to ERA-Interim and ERA5 over the TP region.

Frequency bias (Jerney & Renshaw, 2016) was calculated using surface-CMORPH rainfall observation over a 6-hr period and same threshold (1, 8, and 16 mm) for ERA-Interim, ERA5, and WRF-EnKF simulated rainfall (10- and 30-km) during the summer of 2015. All three simulation experiments (Figures 13a and 13b) overestimated the occurrence of low-threshold events (1 mm) in June, but the EnKF showed the smallest precipitation bias. The occurrence of low-threshold events (1 mm) were underestimated in July and August by EnKF simulation; however, ERA5 simulation captured more accurate low-threshold events regardless of 10- or 30-km horizontal resolution. For frequency bias of 8-mm events (Figures 13c and 13d), it was overestimated in ERA-Interim forecasts at coarse and fine-scale resolution, but EnKF forecasts were close to a perfect score, followed by the ERA5 experiment with a slight overestimation. The noticeable overrepresentativity of 16-mm events was displayed in Figures 13e and 13f for ERA-Interim rainfall at 10- and 30-km grid spacing. With reference to above, ERA5 rainfall only had a slight overestimation while EnKF rainfall closely approached to the observed proportion of high-threshold events at both grids spacing. The frequency bias of different threshold indicating that the WRF-EnKF reanalysis are better than ERA-Interim and ERA5 to capture the intense precipitation events.

Figure 14 shows the evolution of rainfall RMSE from the ERA-I_30, ERA5_30, and EnKF_30 downscale forecasts during the summer of 2015. EnKF_30_6H (EnKF_30_12H) had a smaller RMSE (Figures 14a

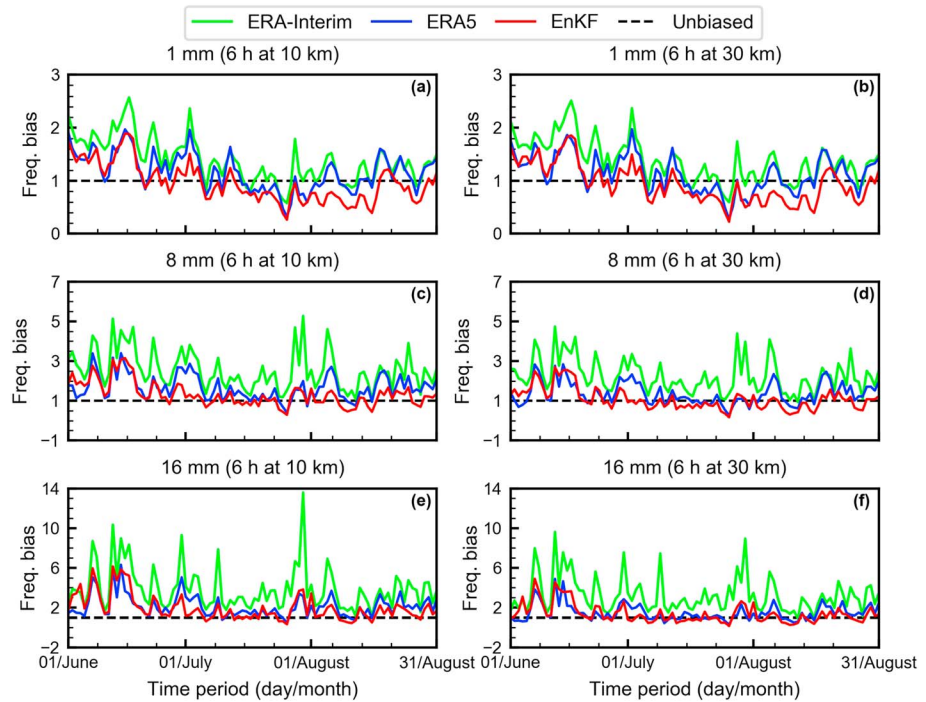


Figure 13. Time evolutions of daily frequency bias of precipitation in the downscaled forecasts driven by ERA-Interim (green), fifth European Centre for Medium-Range Weather Forecasts Reanalysis (ERA5; blue), and Weather Research and Forecasting-ensemble Kalman filter (EnKF; red) reanalysis at 10-km (a, c, and e) and 30-km (b, d, and f) grid spacing over D02. Setting the precipitation thresholds: 1 mm (a, b), 8 mm (c, d), and 16 mm (e, f) over the 6-hr accumulation period.

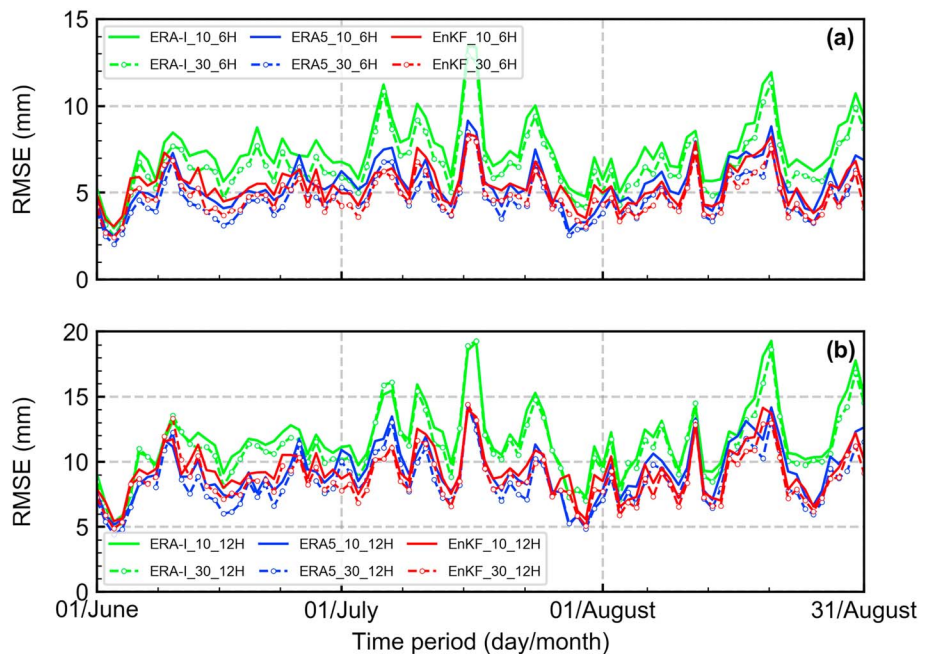


Figure 14. Time evolution of root-mean-square error (RMSE) of the precipitation in the ERA-Interim (green), fifth European Centre for Medium-Range Weather Forecasts Reanalysis (ERA5; blue), and ensemble Kalman filter (EnKF; red) downscaled forecasts (6 and 12 hr) at 10- (bold) and 30-km (dashed and circled) grid spacing over D02.

and 14b) than ERA-I_30_6H (ERA-I_30_12H). However, the performance of EnKF_10_6H (EnKF_10_12H), which was slightly worse than that of EnKF_30_6H (EnKF_30_12H), had a comparable improvement to ERA5_10_6H (ERA5_10_12H). In detail, the rainfall RMSE of WRF-EnKF 6- to 12-hr simulations were larger (June), comparable (July), and smaller (August) than those of ERA5 simulations at 10- and 30-km grid spacing. For three experiments, the rainfall error for the forecasts at the 10-km grid spacing was larger than that of the forecasts at the 30-km grid spacing. Overall, the WRF-EnKF reanalysis had a consistent improvement in rainfall simulations for the whole experiment period compared to ERA-Interim simulations and showed a competitive performance in comparison to ERA5 simulations.

5. Summary and Conclusions

This study evaluated an ensemble-based intermediate-resolution regional reanalysis over the Tibetan Plateau for the summer of 2015 against the soundings with site altitude higher than 1,500 m including intensive radiosonde observations from the TIPEX-III project of China and independent GTS radiosonde observations, as well as the ATOVSL2 satellite sounder observations. Diurnal variations of precipitation were further compared with rainfall observations (surface-CMORPH rainfall) from Chinese Precipitation Analyses for two short-period forecasts that are driven by the ERA-Interim, ERA5, and WRF-EnKF reanalysis at 30- and 10-km grid spacing, respectively.

The experiments showed that the WRF-EnKF reanalysis of Q , T , U , and V approached the observations significantly after only assimilating GTS observations by the PSU WRF-EnKF data assimilation system. Independent verification against the conventional soundings indicates that the WRF-EnKF reanalysis and 6-hr ensemble forecast of specific humidity had a clear advantage over those of ERA-Interim and ERA5 in both spatial and temporal distributions. This result was further confirmed by the verification against satellite sounder observations. The specific humidity of 6- to 12-hr deterministic forecast by downscaling the WRF-EnKF reanalysis produced smaller (comparable) forecast errors than those of ERA-Interim (ERA5). The temperature displayed a comparable performance in different reanalyses or forecasts (ensemble forecasts and downscale forecasts), though the ERA-Interim and ERA5 had advantage in the horizontal wind analysis. However, for 6-hr ensemble forecast and 12-hr deterministic downscale forecast driven by the ensemble analysis and its mean, their wind errors were smaller and grown slower than those by ERA-Interim reanalysis but larger than those by ERA5 reanalysis when only compared with 12-hr deterministic downscale forecast from the WRF-EnKF reanalysis.

The precipitation forecast initialized from the ensemble-based WRF-EnKF reanalysis was more accurate than forecasts using ERA-Interim and ERA5 particularly in terms of precipitation magnitude and spurious rainfall. In addition, the diurnal variation of precipitation of the EnKF-based forecast, which corrected the extreme values of rain rate and reduces the rainfall errors demonstrably, had a clear improvement in comparison to rainfall forecasts from ERA5 and ERA-Interim including the original and downscaled rainfall. The forecast precipitation of WRF-EnKF could more accurately capture the proportion of intense precipitation events based on the frequency bias over 6-hr period. These improvements should come primarily from the benefits of the more accurate WRF-EnKF reanalysis at a higher resolution, which was produced using a state-of-the-art ensemble data assimilation system and a nonhydrostatic regional model.

Despite the WRF-EnKF experiments showing an encouraging performance in specific humidity, precipitation, and diurnal variation of rain rate over the TP by assimilating only conventional observations, the WRF-EnKF reanalyses of temperature and wind may need further improvement compared to ERA5, which assimilated much more observations including radiances from NOAA-18/NOAA-19, METOP-A/METOP-B, and other satellites. Ongoing research seeks to further improve the prototype regional WRF-EnKF system through direct assimilation of all-sky radiances (Minamide & Zhang, 2017, 2018; Zhang et al., 2016). Moreover, a larger domain covering the whole Tibetan Plateau and/or higher-resolution convection-permitting data assimilation (Ying & Zhang, 2018) will be considered for the WRF-EnKF reanalysis in the future study, as well as the use of more advanced assimilation techniques including En3DVar and En4DVar (Zhang et al., 2013; Zhang & Zhang, 2012).

Acknowledgments

The authors thank Yue Ying and Robert Nystrom for their helpful advice and codes. Jie He is supported by the China Scholarship Council. This work is primarily sponsored by the U.S. National Science Foundation (AGS-1712290), the U.S. Department of Energy project WACCEM, the Strategic Priority Research Program of Chinese Academy of Sciences (grant XDA20060401), the Swedish STINT (grant CH2015-6226), the Swedish VR (grant 2017-03780), the Gothenburg Chair Programme for Advanced Studies (GoCAS), and the National Research Foundation of South Korea (grant 2017R1E1A1A03070968). Computer sources from the ADAPT of PSU are provided to run the experiments at the Texas Advanced Computing Center (TACC). The data sets evaluated in this paper are archived and accessible on the stampede2 cluster of TACC (<http://www.tacc.utexas.edu>).

References

Ahn, M.-H., Kim, M.-J., Chung, C.-Y., & Suh, A.-S. (2003). Operational implementation of the ATOVS processing procedure in KMA and its validation. *Advances in Atmospheric Sciences*, 20(3), 398–414. <https://doi.org/10.1007/BF02690798>

Bach, L., Schraff, C., Keller, J. D., & Hense, A. (2016). Towards a probabilistic regional reanalysis system for Europe: Evaluation of precipitation from experiments. *Tellus A: Dynamic Meteorology Oceanography*, 68(1), 32,209. <https://doi.org/10.3402/tellusa.v68.32209>

Bao, X., Luo, Y., Sun, J., Meng, Z., & Yue, J. (2017). Assimilating Doppler radar observations with an ensemble Kalman filter for convection-permitting prediction of convective development in a heavy rainfall event during the pre-summer rainy season of south China. *Science China Earth Sciences*, 60(10), 1866–1885. <https://doi.org/10.1007/s11430-017-9076-9>

Bao, X., & Zhang, F. (2013). Evaluation of NCEP–CFRSR, NCEP–NCAR, ERA-Interim, and ERA-40 reanalysis datasets against independent sounding observations over the Tibetan Plateau. *Journal of Climate*, 26(1), 206–214. <https://doi.org/10.1175/JCLI-D-12-00056.1>

Barker, D. (2005). Southern high-latitude ensemble data assimilation in the Antarctic Mesoscale Prediction System. *Monthly Weather Review*, 133(12), 3431–3449. <https://doi.org/10.1175/MWR3042.1>

Barker, D. M., Huang, W., Guo, Y.-R., Bourgeois, A., & Xiao, Q. (2004). A three-dimensional variational data assimilation system for MM5: Implementation and initial results. *Monthly Weather Review*, 132(4), 897–914. [https://doi.org/10.1175/1520-0493\(2004\)132<0897:ATVDAS>2.0.CO;2](https://doi.org/10.1175/1520-0493(2004)132<0897:ATVDAS>2.0.CO;2)

Berrisford, P., Dee, D., Fielding, K., Fuentes, M., Kallberg, P., Kobayashi, S., & Uppala, S. (2009). *The ERA-interim archive, ERA report series*, (pp. 1–16).

Berrisford, P., Dee, D., Poli, P., Brugge, R., Fielding, K., Fuentes, M., Kallberg, P. et al. (2011). The ERA-Interim archive, version 2.0.

Bormann, N., & Bauer, P. (2010). Estimates of spatial and interchannel observation-error characteristics for current sounder radiances for numerical weather prediction. I: Methods and application to ATOVS data. *Quarterly Journal of the Royal Meteorological Society*, 136(649), 1036–1050. <https://doi.org/10.1002/qj.616>

Chen, D., Tian, Y., Yao, T., & Ou, T. (2016). Satellite measurements reveal strong anisotropy in spatial coherence of climate variations over the Tibet Plateau. *Scientific reports*, 6(1), 30,304. <https://doi.org/10.1038/srep30304>

Chen, D., Xu, B., Yao, T., Guo, Z., Cui, P., & Chen, F. (2015). Assessment of past, present and future environmental changes on the Tibetan Plateau. *Chinese Science Bulletin*.

Chen, X., Pauluis, O. M., & Zhang, F. (2018). Regional simulation of Indian summer monsoon intraseasonal oscillations at gray-zone resolution. *Atmospheric Chemistry Physics*, 18(2), 1003–1022. <https://doi.org/10.5194/acp-18-1003-2018>

Chou, M.-D., & Suarez, M. J. (1999). A solar radiation parameterization for atmospheric studies. *Technical Report*, 15.

Compo, G. P., Whitaker, J. S., Sardeshmukh, P. D., Matsui, N., Allan, R. J., Yin, X., et al. (2011). The twentieth century reanalysis project. *Quarterly Journal of the Royal Meteorological Society*, 137(654), 1–28. <https://doi.org/10.1002/qj.776>

Courtier, P., Thépaut, J. N., & Hollingsworth, A. (1994). A strategy for operational implementation of 4D-Var, using an incremental approach. *Quarterly Journal of the Royal Meteorological Society*, 120(519), 1367–1387. <https://doi.org/10.1002/qj.49712051912>

Curio, J., Maussion, F., & Scherer, D. (2015). A 12-year high-resolution climatology of atmospheric water transport over the Tibetan Plateau. *Earth System Dynamics*, 6(1), 109–124. <https://doi.org/10.5194/esd-6-109-2015>

Dee, D. P., Uppala, S. M., Simmons, A. J., Berrisford, P., Poli, P., Kobayashi, S., et al. (2011). The ERA-Interim reanalysis: Configuration and performance of the data assimilation system. *Quarterly Journal of the Royal Meteorological Society*, 137(656), 553–597. <https://doi.org/10.1002/qj.828>

Ebita, A., Kobayashi, S., Ota, Y., Moriya, M., Kumabe, R., Onogi, K., et al. (2011). The Japanese 55-year reanalysis “JRA-55”: an interim report. *Sola*, 7, 149–152. <https://doi.org/10.2151/sola.2011-038>

Feng, L., & Zhou, T. (2012). Water vapor transport for summer precipitation over the Tibetan Plateau: Multidata set analysis. *Journal of Geophysical Research*, 117, D20114. <https://doi.org/10.1029/2011JD017012>

Gaspari, G., & Cohn, S. E. (1999). Construction of correlation functions in two and three dimensions. *Quarterly Journal of the Royal Meteorological Society*, 125(554), 723–757. <https://doi.org/10.1002/qj.4971255417>

Gelaro, R., McCarty, W., Suárez, M. J., Todling, R., Molod, A., Takacs, L., et al. (2017). The Modern-Era Retrospective Analysis for Research and Applications, version 2 (MERRA-2). *Journal of Climate*, 30(14), 5419–5454. <https://doi.org/10.1175/JCLI-D-16-0758.1>

Gibson, J., Källberg, P., Uppala, S., Hernandez, A., Nomura, A., & Serrano, E. (1997). ERA description. ECMWF Reanalysis Project Report Series 1, Shinfield Park. Reading, United Kingdom, 77.

Harada, Y., Kamahori, H., Kobayashi, C., Endo, H., Kobayashi, S., Ota, Y., et al. (2016). The JRA-55 Reanalysis: Representation of atmospheric circulation and climate variability. *Journal of the Meteorological Society of Japan. Ser. II*, 94(3), 269–302. <https://doi.org/10.2151/jmsj.2016-015>

Hersbach, H., & Dee, D. (2016). ERA5 reanalysis is in production. ECMWF newsletter, No. 147, p7.

Hong, S.-Y., Noh, Y., & Dudhia, J. (2006). A new vertical diffusion package with an explicit treatment of entrainment processes. *Monthly Weather Review*, 134(9), 2318–2341. <https://doi.org/10.1175/MWR3199.1>

Houtekamer, P., & Zhang, F. (2016). Review of the ensemble Kalman filter for atmospheric data assimilation. *Monthly Weather Review*, 144(12), 4489–4532. <https://doi.org/10.1175/MWR-D-15-0440.1>

Houtekamer, P. L., Mitchell, H. L., Pellerin, G., Buehner, M., Charron, M., Spacek, L., & Hansen, B. (2005). Atmospheric data assimilation with an ensemble Kalman filter: Results with real observations. *Monthly Weather Review*, 133(3), 604–620. <https://doi.org/10.1175/MWR-2864.1>

Hu, X. M., Xue, M., McPherson, R. A., Martin, E., Rosendahl, D. H., & Qiao, L. (2018). Precipitation dynamical downscaling over the Great Plains. *Journal of Advances in Modeling Earth Systems*, 10(2), 421–447. <https://doi.org/10.1002/2017MS001154>

Iacono, M. J., Delamere, J. S., Mlawer, E. J., Shephard, M. W., Clough, S. A., & Collins, W. D. (2008). Radiative forcing by long-lived greenhouse gases: Calculations with AER radiative transfer models. *Journal of Geophysical Research*, 113, D13103. <https://doi.org/10.1029/2008JD009944>

Isaksen, I., Bonavita, M., Buizza, R., Fisher, M., Haseler, J., Leutbecher, M., & Raynaud, L. (2010). *Ensemble of data assimilations at ECMWF: European Centre for Medium-Range Weather Forecasts*.

Jermey, P., & Renshaw, R. (2016). Precipitation representation over a two-year period in regional reanalysis. *Quarterly Journal of the Royal Meteorological Society*, 142(696), 1300–1310. <https://doi.org/10.1002/qj.2733>

Joyce, R. J., Janowiak, J. E., Arkin, P. A., & Xie, P. (2004). CMORPH: A method that produces global precipitation estimates from passive microwave and infrared data at high spatial and temporal resolution. *Journal of hydrometeorology*, 5(3), 487–503. [https://doi.org/10.1175/1525-7541\(2004\)005<0487:CAMTPG>2.0.CO;2](https://doi.org/10.1175/1525-7541(2004)005<0487:CAMTPG>2.0.CO;2)

- Kalnay, E., Kanamitsu, M., Kistler, R., Collins, W., Deaven, D., Gandin, L., et al. (1996). The NCEP/NCAR 40-year reanalysis project. *Bulletin of the American Meteorological Society*, 77(3), 437–471. [https://doi.org/10.1175/1520-0477\(1996\)077<0437:TNYRYP>2.0.CO;2](https://doi.org/10.1175/1520-0477(1996)077<0437:TNYRYP>2.0.CO;2)
- Kanamitsu, M., Ebisuzaki, W., Woollen, J., Yang, S.-K., Hnilo, J., Fiorino, M., & Potter, G. (2002). NCEP–DOE AMIP-II Reanalysis (R-2). *Bulletin of the American Meteorological Society*, 83(11), 1631–1644. <https://doi.org/10.1175/BAMS-83-11-1631>
- Kistler, R., Collins, W., Saha, S., White, G., Woollen, J., Kalnay, E., et al. (2001). The NCEP–NCAR 50-year reanalysis: Monthly means CD-ROM and documentation. *Bulletin of the American Meteorological Society*, 82(2), 247–267. [https://doi.org/10.1175/1520-0477\(2001\)082<0247:TNNYRM>2.3.CO;2](https://doi.org/10.1175/1520-0477(2001)082<0247:TNNYRM>2.3.CO;2)
- Kobayashi, S., Ota, Y., Harada, Y., Ebata, A., Moriya, M., Onoda, H., et al. (2015). The JRA-55 reanalysis: General specifications and basic characteristics. *Journal of the Meteorological Society of Japan. Ser. II*, 93(1), 5–48. <https://doi.org/10.2151/jmsj.2015-001>
- Li, J., Wolf, W. W., Menzel, W. P., Zhang, W., Huang, H.-L., & Achtor, T. H. (2000). Global soundings of the atmosphere from ATOVS measurements: The algorithm and validation. *Journal of Applied Meteorology*, 39(8), 1248–1268. [https://doi.org/10.1175/1520-0450\(2000\)039<1248:GSOTAF>2.0.CO;2](https://doi.org/10.1175/1520-0450(2000)039<1248:GSOTAF>2.0.CO;2)
- Lim, K.-S. S., & Hong, S.-Y. (2010). Development of an effective double-moment cloud microphysics scheme with prognostic cloud condensation nuclei (CCN) for weather and climate models. *Monthly Weather Review*, 138(5), 1587–1612. <https://doi.org/10.1175/2009MWR2968.1>
- Lin, C., Chen, D., Yang, K., & Ou, T. (2018). Impact of model resolution on simulating the water vapor transport through the central Himalayas: Implication for models' wet bias over the Tibetan Plateau. *Climate dynamics*, 1–13.
- Liu, X., & Dong, B. (2013). Influence of the Tibetan Plateau uplift on the Asian monsoon-arid environment evolution. *Chinese Science Bulletin*, 58(34), 4277–4291. <https://doi.org/10.1007/s11434-013-5987-8>
- Ma, Y., Kang, S., Zhu, L., Xu, B., Tian, L., & Yao, T. (2008). Tibetan observation and research platform: Atmosphere–land interaction over a heterogeneous landscape. *Bulletin of the American Meteorological Society*, 89(10), 1487–1492.
- Mahmood, S., Davie, J., Jermey, P., Renshaw, R., George, J. P., Rajagopal, E., & Rani, S. I. (2018). Indian monsoon data assimilation and analysis regional reanalysis: Configuration and performance. *Atmospheric Science Letters*, 19(3), e808. <https://doi.org/10.1002/asl.808>
- Mahmood, S., Jermey, P., & Renshaw, R. (2014). Methods for evaluating model performance of IMDAA. Met Office.
- Maussion, F., Scherer, D., Finkelnburg, R., Richters, J., Yang, W., & Yao, T. (2011). WRF simulation of a precipitation event over the Tibetan Plateau, China—An assessment using remote sensing and ground observations. *Hydrology & Earth System Sciences*, 15(6), 1795–1817. <https://doi.org/10.5194/hess-15-1795-2011>
- Maussion, F., Scherer, D., Mölg, T., Collier, E., Curio, J., & Finkelnburg, R. (2014). Precipitation seasonality and variability over the Tibetan Plateau as resolved by the High Asia Reanalysis. *Journal of Climate*, 27(5), 1910–1927. <https://doi.org/10.1175/JCLI-D-13-00282.1>
- Meng, Z., & Zhang, F. (2007). Tests of an ensemble Kalman filter for mesoscale and regional-scale data assimilation. Part II: Imperfect model experiments. *Monthly Weather Review*, 135(4), 1403–1423. <https://doi.org/10.1175/MWR3352.1>
- Meng, Z., & Zhang, F. (2008a). Tests of an ensemble Kalman filter for mesoscale and regional-scale data assimilation. Part III: Comparison with 3DVAR in a real-data case study. *Monthly Weather Review*, 136(2), 522–540. <https://doi.org/10.1175/2007MWR2106.1>
- Meng, Z., & Zhang, F. (2008b). Tests of an ensemble Kalman filter for mesoscale and regional-scale data assimilation. Part IV: Comparison with 3DVAR in a month-long experiment. *Monthly Weather Review*, 136(10), 3671–3682. <https://doi.org/10.1175/2008MWR2270.1>
- Mesinger, F., DiMego, G., Kalnay, E., Mitchell, K., Shafran, P. C., Ebisuzaki, W., et al. (2006). North American regional reanalysis. *Bulletin of the American Meteorological Society*, 87(3), 343–360. <https://doi.org/10.1175/BAMS-87-3-343>
- Minamide, M., & Zhang, F. (2017). Adaptive observation error inflation for assimilating all-sky satellite radiance. *Monthly Weather Review*, 145(3), 1063–1081. <https://doi.org/10.1175/MWR-D-16-0257.1>
- Minamide, M., & Zhang, F. (2018). Assimilation of all-sky infrared radiances from Himawari-8 and impacts of moisture and hydrometeor initialization on convection-permitting tropical cyclone prediction. *Monthly Weather Review*, 146(10), 3241–3258. <https://doi.org/10.1175/MWR-D-17-0367.1>
- Niermann, D., Borsche, M., Kaiser-Weiss, A., Lussana, C., Tveito, O. E., Isotta, F., Jermey, P., et al., (2017). Report for Deliverable 3.8 (D3.8): User friendly synthesis report on evaluation and uncertainty of regional reanalyses. Technical Report, 1–24.
- Onogi, K., Tsutsui, J., Koide, H., Sakamoto, M., Kobayashi, S., Hatsushika, H., et al. (2007). The JRA-25 reanalysis. *Journal of the Meteorological Society of Japan. Ser. II*, 85(3), 369–432. <https://doi.org/10.2151/jmsj.85.369>
- Parrish, D. F., & Derber, J. C. (1992). The National Meteorological Center's spectral statistical-interpolation analysis system. *Monthly Weather Review*, 120(8), 1747–1763. [https://doi.org/10.1175/1520-0493\(1992\)120<1747:TNNCSS>2.0.CO;2](https://doi.org/10.1175/1520-0493(1992)120<1747:TNNCSS>2.0.CO;2)
- Paulson, C. A. (1970). The mathematical representation of wind speed and temperature profiles in the unstable atmospheric surface layer. *Journal of Applied Meteorology*, 9(6), 857–861. [https://doi.org/10.1175/1520-0450\(1970\)09<0857:TMROWS>2.0.CO;2](https://doi.org/10.1175/1520-0450(1970)09<0857:TMROWS>2.0.CO;2)
- Qi, W., Liu, J., & Chen, D. (2018). Evaluations and Improvements of GLDAS2.0 and GLDAS2.1 Forcing Data's Applicability for Basin Scale Hydrological Simulations in the Tibetan Plateau. *Journal of Geophysical Research: Atmospheres*, 123, 13,128–13,148. <https://doi.org/10.1029/2018JD029116>
- Qiu, X. X., & Zhang, F. Q. (2016). Prediction and predictability of a catastrophic local extreme precipitation event through cloud-resolving ensemble analysis and forecasting with Doppler radar observations. *Science China*, 59(3), 518–532. <https://doi.org/10.1007/s11430-015-5224-1>
- Rabier, F., Järvinen, H., Klinker, E., Mahfouf, J. F., & Simmons, A. (2000). The ECMWF operational implementation of four-dimensional variational assimilation. I: Experimental results with simplified physics. *Quarterly Journal of the Royal Meteorological Society*, 126(564), 1143–1170. <https://doi.org/10.1002/qj.49712656415>
- Rienecker, M. M., Suarez, M. J., Gelaro, R., Todling, R., Bacmeister, J., Liu, E., et al. (2011). MERRA: NASA's modern-era retrospective analysis for research and applications. *Journal of Climate*, 24(14), 3624–3648. <https://doi.org/10.1175/JCLI-D-11-00015.1>
- Saslo, S., & Greybush, S. J. (2017). Prediction of lake-effect snow using convection-allowing ensemble forecasts and regional data assimilation. *Weather and Forecasting*, 32(5), 1727–1744. <https://doi.org/10.1175/WAF-D-16-0206.1>
- Shen, Y., Zhao, P., Pan, Y., & Yu, J. (2014). A high spatiotemporal gauge-satellite merged precipitation analysis over China. *Journal of Geophysical Research: Atmospheres*, 119, 3063–3075. <https://doi.org/10.1002/2013JD020686>
- Skamarock, W., Klemp, J., Dudhia, J., Gill, D., Barker, D., Duda, M., et al. (2008). A description of the Advanced Research WRF Version 3. Technical Report, National Center for Atmospheric Research.
- Tao, S., Luo, S., & Zhang, H. (1986). The Qinghai-Xizang Plateau Meteorological Experiment (Qxpmed) May–August 1979. Paper presented at the Proceedings of International Symposium on the Qinghai-Xizang Plateau and Mountain Meteorology, DOI: https://doi.org/10.1007/978-1-935704-19-5_1.
- Uppala, S. M., Kållberg, P. W., Simmons, A. J., Andrae, U., Bechtold, V. D. C., Fiorino, M., et al. (2005). The ERA-40 re-analysis. *Quarterly Journal of the Royal Meteorological Society*, 131(612), 2961–3012. <https://doi.org/10.1256/qj.04.176>

- Wang, A., & Zeng, X. (2012). Evaluation of multireanalysis products with in situ observations over the Tibetan Plateau. *Journal of Geophysical Research*, *117*, D05102. <https://doi.org/10.1029/2011JD016553>
- Weng, Y., & Zhang, F. (2012). Assimilating airborne Doppler radar observations with an ensemble Kalman filter for convection-permitting hurricane initialization and prediction: Katrina (2005). *Monthly Weather Review*, *140*(3), 841–859. <https://doi.org/10.1175/2011MWR3602.1>
- Xu, X., Lu, C., Shi, X., & Gao, S. (2008). World water tower: An atmospheric perspective. *Geophysical Research Letters*, *35*, L20815. <https://doi.org/10.1029/2008GL035867>
- Yang, E.-G., & Kim, H. M. (2017). Evaluation of a regional reanalysis and ERA-Interim over East Asia using in situ observations during 2013–14. *Journal of Applied Meteorology and Climatology*, *56*(10), 2821–2844. <https://doi.org/10.1175/JAMC-D-16-0227.1>
- Yang, E.-G., & Kim, H. M. (2019). Evaluation of short-range precipitation reforecasts from East Asia regional reanalysis. *Journal of Hydrometeorology*, *20*(2), 319–337. <https://doi.org/10.1175/JHM-D-18-0068.1>
- Yang, K., Wu, H., Qin, J., Lin, C., Tang, W., & Chen, Y. (2014). Recent climate changes over the Tibetan Plateau and their impacts on energy and water cycle: A review. *Global Planetary Change*, *112*, 79–91. <https://doi.org/10.1016/j.gloplacha.2013.12.001>
- Yao, T., Xue, Y., Chen, D., Chen, F., Thompson, L., Cui, P., et al. (2019). Recent Third Pole's rapid warming accompanies cryospheric melt and water cycle intensification and interactions between monsoon and environment: Multi-disciplinary approach with observation, modeling and analysis. *Bulletin of the American Meteorological Society*, *100*(3), 423–444. <https://doi.org/10.1175/BAMS-D-17-0057.1>
- Ying, Y., & Zhang, F. (2018). Potentials in improving predictability of multiscale tropical weather systems evaluated through ensemble assimilation of simulated satellite-based observations. *Journal of the Atmospheric Sciences*, *75*(5), 1675–1698. <https://doi.org/10.1175/JAS-D-17-0245.1>
- Ying, Y., Zhang, F., & Anderson, J. L. (2018). On the selection of localization radius in ensemble filtering for multiscale quasigeostrophic dynamics. *Monthly Weather Review*, *146*(2), 543–560. <https://doi.org/10.1175/MWR-D-17-0336.1>
- Yue, Y., & Zhang, F. (2015). An adaptive covariance relaxation method for ensemble data assimilation. *Quarterly Journal of the Royal Meteorological Society*, *141*(692), 2898–2906.
- Zhang, F., Meng, Z., & Aksoy, A. (2006). Tests of an ensemble Kalman filter for mesoscale and regional-scale data assimilation. Part I: Perfect model experiments. *Monthly Weather Review*, *134*(2), 722–736. <https://doi.org/10.1175/MWR3101.1>
- Zhang, F., Minamide, M., & Clothiaux, E. E. (2016). Potential impacts of assimilating all-sky infrared satellite radiances from GOES-R on convection-permitting analysis and prediction of tropical cyclones. *Geophysical Research Letters*, *43*, 2954–2963. <https://doi.org/10.1002/2016GL068468>
- Zhang, F., Snyder, C., & Sun, J. (2004). Impacts of initial estimate and observation availability on convective-scale data assimilation with an ensemble Kalman filter. *Monthly Weather Review*, *132*(5), 1238–1253. [https://doi.org/10.1175/1520-0493\(2004\)132<1238:IOIEAO>2.0.CO;2](https://doi.org/10.1175/1520-0493(2004)132<1238:IOIEAO>2.0.CO;2)
- Zhang, F., & Weng, Y. (2015). Predicting hurricane intensity and associated hazards: A five-year real-time forecast experiment with assimilation of airborne Doppler radar observations. *Bulletin of the American Meteorological Society*, *96*(1), 25–33. <https://doi.org/10.1175/BAMS-D-13-00231.1>
- Zhang, F., Weng, Y., Gamache, J. F., & Marks, F. D. (2011). Performance of convection-permitting hurricane initialization and prediction during 2008–2010 with ensemble data assimilation of inner-core airborne Doppler radar observations. *Geophysical Research Letters*, *38*, L15810. <https://doi.org/10.1029/2011GL048469>
- Zhang, F., Weng, Y., Sippel, J. A., Meng, Z., & Bishop, C. H. (2009). Cloud-resolving hurricane initialization and prediction through assimilation of Doppler radar observations with an ensemble Kalman filter. *Monthly Weather Review*, *137*(7), 2105–2125. <https://doi.org/10.1175/2009MWR2645.1>
- Zhang, F., Zhang, M., & Poterjoy, J. (2013). E3DVar: Coupling an ensemble Kalman filter with three-dimensional variational data assimilation in a limited-area weather prediction model and comparison to E4DVar. *Monthly Weather Review*, *141*(3), 900–917. <https://doi.org/10.1175/MWR-D-12-00075.1>
- Zhang, M., & Zhang, F. (2012). E4DVar: Coupling an ensemble Kalman filter with four-dimensional variational data assimilation in a limited-area weather prediction model. *Monthly Weather Review*, *140*(2), 587–600. <https://doi.org/10.1175/MWR-D-11-00023.1>
- Zhang, M., Zhang, F., Huang, X.-Y., & Zhang, X. (2011). Intercomparison of an ensemble Kalman filter with three- and four-dimensional variational data assimilation methods in a limited-area model over the month of June 2003. *Monthly Weather Review*, *139*(2), 566–572. <https://doi.org/10.1175/2010MWR3610.1>
- Zhang, Q., Pan, Y., Wang, S., Xu, J., & Tang, J. (2017). High-resolution regional reanalysis in China: Evaluation of 1 year period experiments. *Journal of Geophysical Research: Atmospheres*, *122*, 10,801–10,819. <https://doi.org/10.1002/2017JD027476>
- Zhang, R., Jiang, D., Zhang, Z., & Yu, E. (2015). The impact of regional uplift of the Tibetan Plateau on the Asian monsoon climate. *Palaeogeography, Palaeoclimatology, Palaeoecology*, *417*, 137–150. <https://doi.org/10.1016/j.palaeo.2014.10.030>
- Zhang, R., Koike, T., Xu, X., Ma, Y., & Yang, K. (2012). A China-Japan cooperative JICA atmospheric observing network over the Tibetan Plateau (JICA/Tibet Project): An overview. *Journal of the Meteorological Society of Japan. Ser. II*, *90*, 1–16.
- Zhang, Y., Zhang, F., & Stensrud, D. J. (2018). Assimilating all-sky infrared radiances from GOES-16 ABI using an ensemble Kalman filter for convection-allowing severe thunderstorms prediction. *Monthly Weather Review*, *146*(10), 3363–3381. <https://doi.org/10.1175/MWR-D-18-0062.1>
- Zhao, P., Xu, X., Chen, F., Guo, X., Zheng, X., Liu, L., et al. (2018). The third atmospheric scientific experiment for understanding the Earth–Atmosphere coupled system over the Tibetan Plateau and its effects. *Bulletin of the American Meteorological Society*, *99*(4), 757–776. <https://doi.org/10.1175/BAMS-D-16-0050.1>
- Zhou, X., Yang, K., & Wang, Y. (2018). Implementation of a turbulent orographic form drag scheme in WRF and its application to the Tibetan Plateau. *Climate dynamics*, *50*(7–8), 2443–2455. <https://doi.org/10.1007/s00382-017-3677-y>